Quantum embedding methods for correlated excited states of point defects: Case studies and challenges

Lukas Muechler,[1] Danis I. Badrtdinov,[1,2] Alexander Hampel,[1] Jennifer Cano,[1,3] Malte Rösner,[4] and Cyrus E. Dreyer[1,3]

[1]*Center for Computational Quantum Physics, Flatiron Institute, 162 5th Avenue, New York, New York 10010, USA*
[2]*Theoretical Physics and Applied Mathematics Department, Ural Federal University, 620002 Yekaterinburg, Russia*
[3]*Department of Physics and Astronomy, Stony Brook University, Stony Brook, New York 11794-3800, USA*
[4]*Institute for Molecules and Materials, Radboud University, Heijendaalseweg 135, 6525 AJ Nijmegen, Netherlands*

(Received 1 June 2021; accepted 17 May 2022; published 6 June 2022)

A quantitative description of the excited electronic states of point defects and impurities is crucial for understanding materials properties, and possible applications of defects in quantum technologies. This is a considerable challenge for computational methods, since Kohn-Sham density functional theory (DFT) is inherently a ground-state theory, while higher-level methods are often too computationally expensive for defect systems. Recently, embedding approaches have been applied that treat defect states with many-body methods, while using DFT to describe the bulk host material. We implement such an embedding method, based on Wannierization of defect orbitals and the constrained random-phase approximation approach, and perform systematic characterization of the method for three distinct systems with current technological relevance: a carbon dimer replacing a B and N pair in bulk hexagonal BN (C_BC_N), the negatively charged nitrogen-vacancy center in diamond (NV^-), and an Fe impurity on the Al site in wurtzite AlN (Fe_{Al}). In the context of these test-case defects, we demonstrate that crucial considerations of the methodology include convergence of the bulk screening of the active-space Coulomb interaction, the choice of exchange-correlation functional for the initial DFT calculation, and the treatment of the "double-counting" correction. For C_BC_N we show that the embedding approach gives many-body states in agreement with analytical results on the Hubbard dimer model, which allows us to elucidate the effects of the DFT functional and double-counting correction. For the NV^- center, our method demonstrates good quantitative agreement with experiments for the zero-phonon line of the triplet-triplet transition. Finally, we illustrate challenges associated with this method for determining the energies and orderings of the complex spin multiplets in Fe_{Al}.

DOI: 10.1103/PhysRevB.105.235104

I. INTRODUCTION

Point defects, such as vacancies, interstitial atoms, antisites, and atomic impurities, are ubiquitous in all materials. Even when present in minute concentrations, they can profoundly alter material and device properties. Defects are often detrimental to device performance; for example, so-called Shockley-Read-Hall (SRH) [1,2] defect-mediated recombination of electrons and holes in semiconductors is a key efficiency-limiting process in solar cells and light-emitting diodes. However, more recently, defects have emerged as robust and manipulatable quantum systems for the next generation of quantum technologies, e.g., spin qubits for quantum computing [3–6], single-photon emitters (SPEs) for quantum communication [7,8], and nanoprobes for quantum metrology [9].

In both contexts, the properties of the *electronic excited states* of the defect play a key role. For quantum applications, manipulation of the spin-qubit state for computing is often carried out via optical excitation, and relies on specific nonradiative transitions from the excited state (i.e., intersystem crossings [10,11]). Also, whether or not a defect will be appropriate as a SPE depends on the electron-phonon coupling of the defect in its excited state [7]. Finally, nanometrology with defects often relies on the dipole moment or magnetic properties of the excited states [9]. Point-defect excited states also play an important role when considering their detrimental effect on the host material, for example resulting in additional channels for SRH in wide-band-gap insulators [12,13].

Thus, a quantitative theoretical understanding of the electronic excited states of defects is crucial. However, describing defect excited states from first-principles is a significant challenge. Kohn-Sham density functional theory (KS-DFT), which is the workhorse for determining defect properties [14,15], is a ground-state theory, and the calculated eigenvalues do not correspond to the quasiparticle addition/removal energies [16–18]. As is the case for atoms or molecules, the excited states may correspond to multiplets that cannot be described by a single-Slater-determinant theory like KS-DFT [19,20].

This motivates the use of higher-level many-body methods to treat defect excited states; however, defects are a challenging application for such methods, due to computational expense. Specifically, in order to model an isolated defect,

large "supercells" are necessary to separate defects from their periodic images; if open boundary conditions are used, then large clusters are required to converge to a bulk-like environment for the defect.

The computational problem of treating a small "active space" of correlated defect states within a relatively weakly correlated bulk (i.e., supercell or cluster) is thus ideal for a quantum embedding approach [21,22]. Such approaches have enjoyed extensive success in quantum chemistry [22–37] and solid-state physics [21,38–40] for treating strongly correlated materials and molecules. Recently, their popularity for treating defects [41–46] and other inhomogeneous systems [47–55] has increased rapidly.

For the case of defects in semiconductors and insulators, the methodology demonstrated first by Bockstedte *et al.* [42], and then implemented and developed by other groups [41,43–46], is particularly promising. This approach combines the state-of-the-art and highly successful methods for DFT calculations of defects in semiconductors [15] with downfolding and embedding approaches tailored to solid-state systems [38–40,56]. Specifically, the foundation for this embedding approach [41–44] is a DFT calculation of the defect in a periodic supercell, which avoids the challenges associated with finite clusters sometimes used in quantum chemistry implementations, including quantum confinement effects and interactions between defect wave functions and the cluster surface (see Ref. [15] for discussion of supercells versus clusters). The choice of DFT is also found to be a much better starting point for such systems compared to Hartree-Fock, which is widely used in quantum chemistry implementations. Also, the active space is chosen to be minimal, and a screened Coulomb interaction is used in that space; this is often the preferred approach in solid-state embedding [38–40,56], as opposed to increasing the size of the active space with a bare Coulomb interaction towards convergence (see, e.g., Ref. [57]). Owing to the small size of the Hilbert space, our method can serve as the basis for developing simplified effective models that capture qualitative and quantitative aspects of the defect system.

One of the key challenges of embedding methods is developing a quantitatively accurate *ab initio* procedure for downfolding onto the active space; careful treatment of the details by which the DFT calculation in the bulk is combined with the many-body (MB) calculation in the active subspace is crucial for accurate final observables. These details include: (i) the choice of the initial electronic configuration on which to base the embedding methodology; (ii) the procedure for isolating the correlated orbitals from the bulk; (iii) the approach for obtaining the effective Coulomb interaction in the subspace [41,56,58]; and (iv) the approach to remove "double-counting" errors of the Coulomb interaction as a result of the DFT starting point [59,60].

In this paper we will explore these issues with the goal of developing quantum embedding techniques [41,42] for quantitative prediction of defect properties in a variety of systems. To this end, we perform calculations on three diverse test-case defects, with a focus on systematic characterization of the methodological details (i)–(iv) above. The first is a carbon dimer replacing a boron and nitrogen atom (C_BC_N) in bulk hexagonal BN, whose simple electronic structure will allow comparison of the results to model calculations. The second is the NV^- center in diamond, which is the prototypical correlated defect, and will serve as a benchmark against experiment and other computational techniques. The third is an iron atom replacing aluminum in AlN (Fe_{Al}), which will serve as a stringent test of the methodology on a defect where correlations play a key qualitative role.

The rest of the paper is organized as follows: in Sec. II we introduce the case-study defects, the detailed motivation for choosing them, and their electronic structure; Section III provides a brief outline of the general embedding approach; we analyze in detail the aspects of the methodology mentioned above in the context of our test-case defects in Sec. IV; in Sec. V we discuss some additional aspects of the methodology, including how to quantify the correlated nature of the MB states and how our method can be used to generate simplified models; we conclude the paper in Sec. VI.

II. CASE-STUDY DEFECTS

In this section, we will briefly introduce the case-study defects, their electronic structure, and the motivation for why they were chosen for this study. Computational parameters for each defect can be found in Sec. S1 of the Supplemental Material (SM) [61] .

In terms of notation, single-particle defect states will be referred to with lower case letters indicating the irreducible representation (irrep) of the defect's point group that they transforms as; for example, a single-particle state that is fully symmetric will be referred to as a_1. MB states will also be referred to by their orbital symmetry, but with upper case letters and a leading superscript indicating their spin multiplicity (i.e., $2S+1$); for example, a fully symmetric triplet state will be referred to as $|^3A_1\rangle$ (the ket notation indicates that the MB states represent linear combinations of Fock states). Note that we will not treat spin-orbit coupling in this paper, so this decomposition into orbital and spin symmetry is well defined. For discussing single Fock states, we will adopt the following convention:

$$|\overline{\phi_1\phi_2\ldots\phi_{N_{\rm orb}}};\phi_1\phi_2\ldots\phi_{N_{\rm orb}}\rangle = \prod_i c^\dagger_{i\downarrow}\prod_j c^\dagger_{j\uparrow}|0\rangle, \qquad (1)$$

where $|0\rangle$ is the vacuum, $N_{\rm orb}$ is the number of orbitals, ϕ_i labels the defect spin-orbital, and is either 0 or 1 indicating the occupancy of the basis spin-orbital state, the overbar indicates spin down, and $c^\dagger_{i\downarrow}$ ($c^\dagger_{j\uparrow}$) only appears on the right-hand side when $\overline{\phi_i}=1$ ($\phi_j=1$).

A. C_BC_N in bulk hexagonal BN: A simple model

C_BC_N in hexagonal BN has attracted significant recent attention, as it was proposed as the origin of the 4.1 eV zero-phonon line [62–64] (ZPL, see Sec. IV B) single-photon emitter observed in BN based on the energetics of emission [65], and calculations of photoluminescence lineshapes [66,67]. For our purposes, C_BC_N was chosen as it has a particularly simple electronic structure that can be compared to analytical calculations.

As a host material, we will consider bulk $P6_3/mmc$, i.e., three-dimensional layered BN [see Fig. 1(c) for example

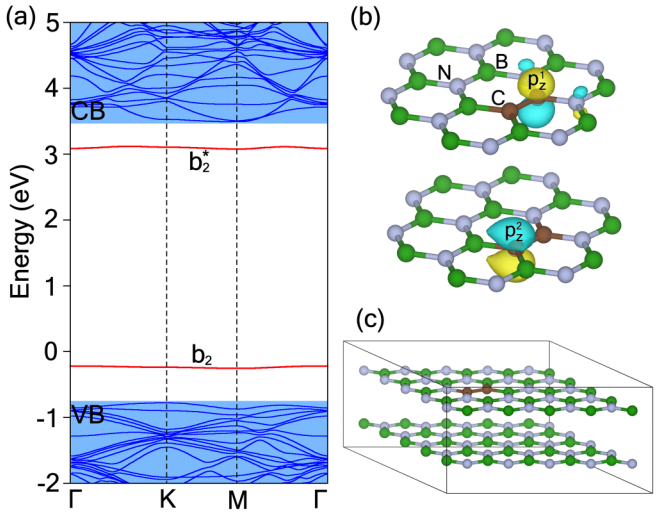

FIG. 1. (a) DFT Band structure for C_BC_N in bulk-layered BN calculated with the PBE functional (neglecting spin). Defect states are highlighted with red color and denoted with symmetry labels; bulk bands are blue. (b) The carbon p_z-character Wannier functions used to define the active space. (c) Example of bulk BN supercell.

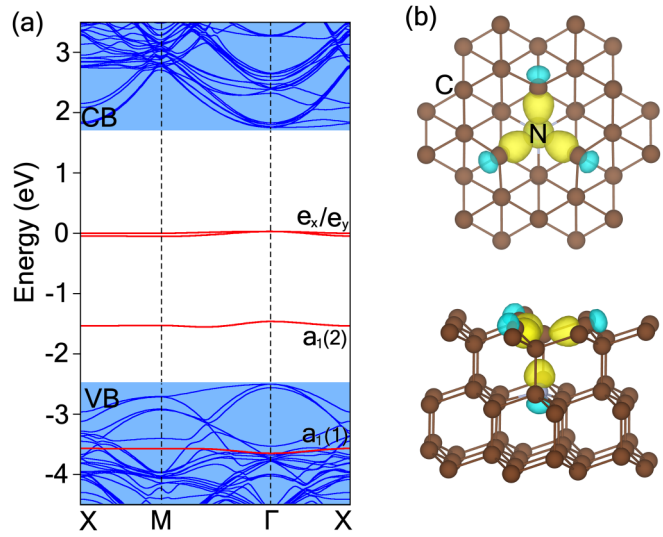

FIG. 2. (a) Band structure for NV^- center in diamond calculated with the PBE functional (neglecting spin). Defect states are highlighted with red color and denoted with symmetry labels, the bulk bands in blue. (b) The maximally-localized Wannier functions plotted in top and side view are shown for the sp^3 dangling bonds of N and C atoms, which were used to define the active space.

supercell]. Replacing a nearest neighbor B and N pair with a neutral C dimer results in two defect states within the band gap of BN. These states are of bonding and anti-bonding character resulting from corresponding combinations of C p_z orbitals [65], c.f., Fig. 1(a). We label these states b_2 and b_2^*, respectively, using the irreps of the C_{2v} point group of the defect, and use them as the active space. The defect MB states can correspondingly be expressed in two equivalent bases: $|\overline{b_2 b_2^*}; b_2 b_2^*\rangle$, which we call the band basis, since it corresponds to the basis of Kohn-Sham bands; and $|\overline{p_z^2 p_z^1}; p_z^2 p_z^1\rangle$, which we refer to as the orbital basis, since it will be the localized Wannier basis we use [see Fig. 1(b) and Sec. IV C]. As discussed in Sec. V B, calculations in these bases are equivalent, but the physical interpretation as well as the development of simplified models may be more transparent for a given choice.

Based on comparison with the simple model of a Hubbard dimer (see Sec. S2A1 of the SM [61]), we expect six MB states, all with A_1 orbital symmetry, in the following energetic ordering. The ground state is a singlet, which we label as $|^1A_1\rangle$, and roughly corresponds to two electrons in the bonding b_2 orbital. The first set of excited states is a spin triplet manifold $|^3A_1\rangle$, which involves exciting an electron from b_2 to b_2^* (both electrons with the same spin). The next excited state is an open-shell singlet which we denote $|^1A_1'\rangle$, where the excited electron has opposite spin to the one in b_2. Finally, there is an additional excited-state singlet, which we denote $|^1A_1''\rangle$, which involves the excitation of both electrons to b_2^*. More details of these states are given in Sec. S2A of the SM [61], including a review of DFT calculations for the excited states via the delta self-consistent field (ΔSCF) method.

B. NV^- in diamond: An experimental benchmark

The negatively-charged nitrogen-vacancy center in diamond (NV^-) is the prototypical deep defect for quantum technologies [10]. The motivation to choose it for this study is that it is extremely well-characterized experimentally, and with a variety of theoretical methods. Thus it has become a standard for experimental verification of theories for correlated defect states (for reviews see, e.g., Refs. [7–10,68,69]).

The NV^- center consists of a C vacancy in diamond with a N substituting a nearest-neighbor C atom. The defect states consist of dangling sp^3 bonds from the carbons and nitrogen atoms around the vacancy [70,71]. Linear combinations of these dangling bonds results in the single-particle defect states shown in Fig. 2(a). Three states are in the bulk band gap, labeled by their irreps of the C_{3v} point group as $a_1(2)$ (which is doubly occupied) and e (which is twofold degenerate, also occupied by two electrons). There is another doubly-occupied $a_1(1)$ state resonant with the valence band (VB).

As with C_BC_N, we will consider two bases for constructing MB states. In this case, the band basis will be labeled by the irreps of the Kohn-Sham states $|\overline{e_x e_y a_1(2) a_1(1)}; e_x e_y a_1(2) a_1(1)\rangle$, while the orbital basis will consists of the sp^3 dangling bonds of the carbons next to the vacancy (labelled 1-3) and the N: $|\overline{sp^3_{C_1} sp^3_{C_2} sp^3_{C_3} sp^3_N}; sp^3_{C_1} sp^3_{C_2} sp^3_{C_3} sp^3_N\rangle$ [see Fig. 2(b)].

The MB states of NV^-, as determined from symmetry considerations and orbital models [71], experiment [70], and previous calculations [42,43,72], consist of: a ground state triplet $|^3A_2\rangle$, represented by aligned spins on e_x and e_y; an excited state singlet $|^1E_1\rangle$ from flipping one of the spins in the e states; and an excited state singlet $|^1A_1\rangle$ and triplet $|^3E\rangle$ resulting from exciting an electron from $a_1(2)$ to the e manifold. Only the fully symmetric atomic configuration of $|^3E\rangle$ is considered in this paper, i.e., we neglect the small energy reduction from the Jahn-Teller splitting of that degenerate state [73]. See Sec. S3 of the SM [61] for details on how we calculate the symmetry of the MB states. More details on the MB states, including a review of DFT calculations for the

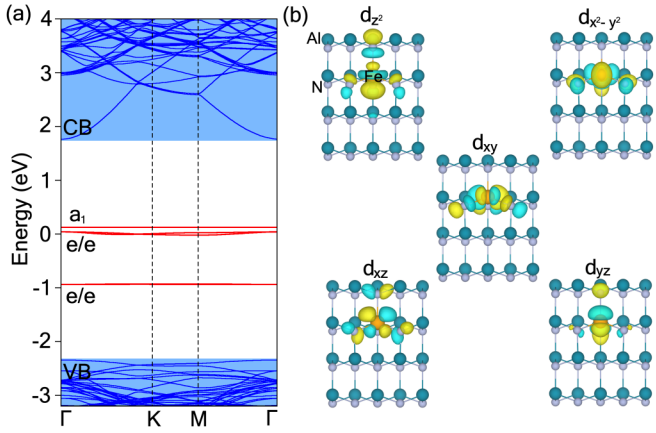

FIG. 3. (a) Band structure for Fe_{Al} in wurtzite AlN calculated with the PBE functional (neglecting spin). Defect states are highlighted with red color and denoted with symmetry labels, the bulk bands in blue. (b) The Wannier functions for $3d$ orbitals, which were used to define the active space.

excited states via the ΔSCF method, are given in Sec. S2B of the SM [61].

C. Fe_{Al} in AlN: A challenging correlated state

The final defect we will consider in this study is an Fe atom substituted on an Al site (Fe_{Al}) in wurtzite AlN (Fig. 3). In general, transition-metal (TM) impurities in semiconductors and insulators have been widely studied as both detrimental and functional defects; e.g., Cu and Au are notorious deep traps/SRH recombination centers in Si [74], while Cr in Al_2O_3 is the famous color center responsible for the red emission of ruby [75]. Often, transition-metal impurities have an open d shell, and thus a rich structure of multiplet excited states, which may be interesting for spin qubits.

The reason that we chose Fe_{Al} for this study is that it represents a significantly more complex electronic structure than both C_BC_N and NV^-. As we will show, rather than correlations renormalizing the single-particle picture, they qualitatively change the nature of the states. At the same time, the relevant defect states reside inside of the band gap. This removes effects of disentanglement, which we will not discuss in detail in this paper.

We will focus on the neutral charge state of Fe_{Al}, which was found to be the lowest energy for Fermi levels near the mid gap of AlN [76]. In this case, Fe exists in the 3+ oxidation state, and thus has five electrons in its $3d$ states. The point symmetry of Fe_{Al} in wurtzite AlN is C_{3v}. The nearest neighbors around the Fe atom are four N atoms arranged in a tetrahedron, with the bond along the threefold axis (crystallographic c direction) slightly larger than the other three by ∼0.5%. It is often assumed that the symmetry lowering from the perfectly tetrahedral T_d symmetry (all bonds the same length) has a small effect on the splitting of the states, and thus the symmetry degeneracies can be analyzed in terms of the irreps of T_d.

The T_d crystal field splits the Fe d orbitals into a lower-energy, doubly degenerate e manifold, and a higher-energy t_2 manifold. The lower-symmetry C_{3v} crystal field of wurtzite AlN splits the t_2 states into e and a_1 states [Fig. 3(a)]. Without spin polarization, these states are in the band gap near the VB, as shown in Fig. 3 (note that including spin polarization significantly changes the nature of the states [76], as discussed in Sec. IV A and in Sec. S2C of the SM [61]). Thus the basis for studying Fe_{Al} is simply these $3d$ states: $|\overline{d_{z^2}d_{xz}d_{yz}d_{x^2-y^2}d_{xy}}; d_{z^2}d_{xz}d_{yz}d_{x^2-y^2}d_{xy}\rangle$.

For the other test-case defects, we knew exactly the nature of the MB states that we should find in our embedding calculations. However Fe_{Al} is much less explored theoretically and experimentally, and thus serves as a test of the predictive power of our method. Still, we can use ligand field theory for a general d^5 ion in a T_d crystal field as the basis of our expectations for the MB states [76–80] (see Fig. S1 in the SM [61] for the predicted splitting and degeneracies). In this picture, the nature of the ground and excited states is determined by the magnitude of the crystal-field splitting (CFS).

For relatively small CFS, the ground state is a sixfold degenerate spin 5/2 state with A_1 orbital symmetry (denoted $|^6A_1\rangle$) that originates from the high-spin $|^6S\rangle$ ground state of the free atom. The low-lying excited states are spin 3/2, originating from the 36-fold degenerate $|^4G\rangle$ manifold in the free atom. In the T_d crystal field, they split into: $|^4T_1\rangle$, $|^4T_2\rangle$, $|^4E\rangle$, and $|^4A_1\rangle$ [77–79]; in C_{3v}, the $|^4T_1\rangle$ ($|^4T_2\rangle$) states split into $|^4E\rangle$ and $|^4A_2\rangle$ ($|^4A_1\rangle$). For large CFS (and T_d), the ground state becomes a spin 1/2 $|^2T_2\rangle$ state, and the low-energy excited states may include various other spin 1/2 states originating from the $|^2I\rangle$ manifold of the free atom (in addition to the spin 3/2 states).

It has been experimentally demonstrated [78–80] that Fe_{Ga} in GaN in the neutral charge state has a high-spin $S = 5/2$ ground state, and all theoretical [76,81] (see also Sec. S2C2 of the SM [61]) and experimental [82–84] work on Fe_{Al} in AlN indicate that it should be the same. As we will see in Sec. IV F, determining the ground state to be high spin versus low spin is a sensitive quantitative test of our methodology.

More details on the MB states, including a review of DFT calculations for the excited states via the ΔSCF method, are given in Sec. S2C of the SM [61].

III. GENERAL APPROACH

Now that we have introduced our case-study defects, we will give a brief outline of the methodology. In Sec. IV, each step will be discussed in detail, in the context of our test-case defects.

The standard method for treating isolated point defects in semiconductors and insulators via DFT calculations is to construct a supercell with a large amount of host material to separate the defect from its periodic images [15,85,86]. In this context, the goal of the quantum embedding approach for defects [42,43] is to treat the host semiconductor at the DFT level, while using a MB method (i.e., one that can handle the possibility of correlated, multideterminant states) to treat the electronic structure of the defect. To do this, the Bloch states related to the defect are isolated from the bulk-like states, and transformed to a localized basis via Wannierization (see Sec. IV C). The defect states are treated as a "correlated

subspace" with the Hamiltonian

$$H = -\sum_{ij,\sigma}(t_{ij}c^{\dagger}_{i\sigma}c_{j\sigma} + \text{H.c.}) + \frac{1}{2}\sum_{ijkl,\sigma\sigma'} U_{ijkl}c^{\dagger}_{i\sigma}c^{\dagger}_{j\sigma'}c_{l\sigma'}c_{k\sigma} - H_{\text{DC}} - \mu\sum_{i,\sigma} c^{\dagger}_{i\sigma}c_{i\sigma}, \quad (2)$$

where σ, σ' indicate spin and i, j, k, l correspond to defect-related states; t_{ij} are the hopping matrix elements between defect states in our Wannier basis (Sec. IV C); U_{ijkl} are the Coulomb matrix elements in the correlated subspace, screened by the rest of the states in the supercell (Sec. IV D); H_{DC} is a "double-counting" correction for the Coulomb interaction included in t_{ij} (Sec. IV F); and μ is a chemical potential used to enforce the nominal occupation of the defect states. Only neutral excitations are considered here, i.e., we do not consider ionization of the defect. By utilizing localized Wannier functions to describe the correlated subspace, we can restrict ourselves to the minimum of involved correlated states. The impurity-bulk "connection" is thereby established in two ways. First, the properties of the Wannier orbitals are controlled by the impurity geometry within the host material. Second, the Coulomb matrix elements are screened by the host environment.

For the defects described in this paper, the number of spin-orbitals in the correlated subspaces are quite modest, ranging from four for C_BC_N to ten for Fe_{Al}. Thus, Eq. (2) can be exactly diagonalized (i.e., the full configuration interaction can be used [42,43]). In the following sections we outline the methodology to determine the parameters in Eq. (2) and ultimately solve for the MB states.

Details of the computational parameters are provided in Sec. S1 of the SM [61]. All DFT calculations are performed using the VASP code [87–89], and Wannierization is performed via the interface to WANNIER90 [90]. The screened Coulomb matrix elements are calculated using the constrained random-phase approximation capabilities of VASP [91] (see Sec. IV D). The exact diagonalization is performed with tools in the TRIQS [92] library.

The strengths of this approach are twofold. First, it leverages the extremely well-developed tools in the fields of DFT approaches for defects in semiconductors [15], as well as solid-state embedding methods like DFT + dynamical mean-field theory (DMFT) [38] and similar approaches [93]. Second, each step utilizes capabilities in widely available codes, which allows for simple reproduction and extension of our results and methodology.

IV. METHODOLOGICAL DETAILS AND LESSONS FROM TEST CASES

In this section, we will expand upon various aspects of the embedding methodology outlined in Sec. III, using the test-case defects introduced in Sec. II. In particular, we will focus on the crucial details described in Sec. I: (i) basic aspects of the initial DFT calculation on which the embedding is based (Sec. IV A), including the choice of exchange-correlation functional (Sec. IV E) and the treatment of atomic relaxations in the ground and excited states (Sec. IV B); the downfolding procedure, i.e., (ii) the Wannierization (Sec. IV C) and (iii) calculation of the screened Coulomb interaction (Sec. IV D); and (iv) the Coulomb double-counting (DC) problem resulting from joining DFT and exact diagonalization (Sec. IV F).

A. Initial DFT electronic structure for defect geometries and the noninteracting Hamiltonian

We begin our analysis of the general methodology described in Sec. III with the initial DFT calculation of the defective supercell, on which the rest of the procedure is based. The role of the initial DFT calculation in the embedding procedure is three-fold: (a) to obtain an accurate atomic geometry for the defect; (b) to provide the bulk band structure as needed to evaluate the screening of interaction matrix elements U_{ijkl} in the active space (see Sec. IV D); and (c) to provide the single-particle terms t_{ij} of Hamiltonian in the active space given in Eq. (2). The challenge for embedding approaches for defects is to balance these aspects, i.e., obtaining an accurate electronic and atomic structure, as well as an appropriate noninteracting starting point for the embedding method.

For example, many defects are paramagnetic, i.e., they have nonzero spin. However, for the Hamiltonian in Eq. (2), the exchange interaction is accounted for in the interaction term (second line), and should not be included in the hopping matrix elements t_{ij}. Also, exchange-correlation (XC) functionals such as HSE [94,95] are expected to result in more accurate band gaps [96], which would translate to more accurate bulk screening, and possibly more accurate defect geometries [15], but HSE will also increase the Coulomb interaction effectively included in t_{ij}, which must be accounted for in the DC term in Eq. (2). The corresponding discussion on the impact of functional choices is given in Sec. IV E, where we will compare results with the initial DFT calculation performed with PBE [97] semilocal generalized-gradient approximation (GGA) and HSE [94,95] hybrid functionals.

In order to strike this balance between accurate structural parameters and a good noninteracting starting point, we will use the following procedure for the initial DFT calculations. First, atomic relaxations are performed using the standard procedure [15], i.e., spin polarization is included and a finite $2 \times 2 \times 2$ Γ-centered k mesh is used to preserve the symmetry in defects/hosts with hexagonal symmetry. This is intended to obtain an accurate defect structure. Afterwards, with the geometry fixed, an additional nonspinpolarized calculation is performed. From this calculation, we will obtain all necessary hopping and Coulomb interaction matrix elements for the MB Hamiltonian, as discussed in the next sections.

In certain cases, there may be different options for the initial spinless electronic configuration. Considering our case-study defects, C_BC_N is completely unambiguous: Since the single particle ground state involves one doubly occupied defect band [two electrons in b_2, see Fig. 1(a)] the initial DFT calculation is identical whether or not spin is included. For NV^-, the ground state contains a half-filled e manifold, which would form a spin triplet in the spinfull case. In principle there are different options for constructing an initial spinless state,

though the straightforward choice is one (spinless) electron in each e orbital to preserve the symmetry. We find that the electronic structure of this state is very similar to the triplet state. For example, relaxing the geometry of the defect with or without spin results in identical structures (differences less than 3×10^{-3} Å).

Fe_{Al} in AlN is a case where including spin polarization in the DFT calculations significantly changes the electronic structure. It was shown in Ref. [76] that when spin is included in the calculation, the $S = 5/2$ ground state has a large splitting (∼10 eV) between the unoccupied spin-minority Fe $3d$ states and the occupied spin-majority Fe $3d$ states; a spinless calculation results in all Fe $3d$ states in the band gap of AlN [see Fig. 3(a)]. Since these states should be filled by five electrons, the occupations in the spinless calculation will be four electrons in the lower-energy e states, and $1/2$ of an electron in each of the higher-energy e states that are slightly split from the a_1 state by the C_{3v} crystal field [see Fig. S2(a) in the SM [61]. This is the electronic structure that we use to obtain the noninteracting part of our MB Hamiltonian. One could also consider attempting to construct a spinless initial state that is closer to the spin-polarized structure, e.g., by constraining the occupation of the Fe $3d$ Kohn-Sham states such that all five are half filled, see Fig. S2(b) in the SM [61]. However, this constrained occupation is somewhat at odds with the spirit of Eq. (2), where the DFT calculations are intended to approximate a noninteracting calculation. We discuss in detail the effects of choosing different initial occupations in Sec. S2C1 of the SM [61].

B. Structural relaxation in excited states for the zero-phonon line

One of the key experimental observables from optical measurements on defects is the "zero-phonon line" (ZPL) energy [98,99], which corresponds to a relatively sharp spectral line (for cases of weak to moderate electron-phonon coupling [100]) at the high-energy threshold for luminescence, or equivalently, the low-energy threshold for absorption (see Fig. 4). The ZPL corresponds to the transition energy between the excited and ground state, each at their equilibrium atomic structure. Below, we will show ZPL results for C_BC_N and NV^- in order to compare with experiments and previous calculations.

At present, we do not have a way of performing atomic relaxations in the excited state, so we resort to the standard method [14] of performing a constrained DFT (cDFT) calculation to approximate the electronic structure of the excited state, and then relaxing the atoms under the constraint. Once we have an approximation for the structure of the excited state, we then find the difference between MB energies calculated for the ground and excited state structures ΔE_{MB} (i.e., the difference in the vertical absorption and emission energies in Fig. 4). This gives us the sum of the Frank-Condon (FC) relaxation energy in the excited and ground states, $E_g^{\mathrm{FC}} + E_e^{\mathrm{FC}}$ (see Fig. 4). We assume that these relaxation energies are equal, and thus $E_g^{\mathrm{FC}} = E_e^{\mathrm{FC}} = \Delta E_{\mathrm{MB}}/2$, which is quite accurate for C_BC_N [65] and NV^- [101].

For C_BC_N, we are interested in the $|^1A_1\rangle \rightarrow |^1A_1'\rangle$ transition, since it is the one attributed to the 4.1 eV ZPL in experiment [65]. Approximating the excited state $|^1A_1'\rangle$ is achieved by populating the b_2^* antibonding orbital with one electron taken from the b_2 bonding orbital. The key observable for the NV^- center is its 1.945 eV ZPL corresponding to transitions between $|^3A_2\rangle$ and $|^3E\rangle$ [10], which allows for a quantitative test of the methodology. The excited state triplet $|^3E\rangle$ is approximated by promoting an electron from $a_1(2)$ to the e manifold [see Fig. 2(a)]. In order to avoid the Jahn-Teller distortion and remain in the C_{3v} symmetric structure, the electron density is spread between the e states [101].

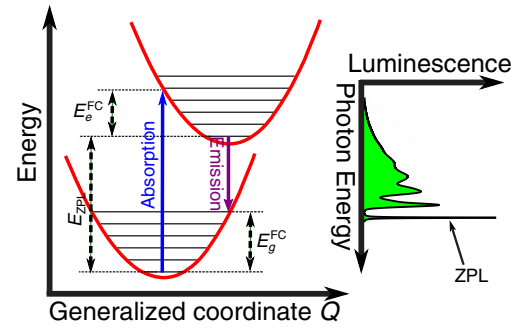

FIG. 4. Schematic of the one-dimensional configuration-coordinate picture of optical absorption and emission transitions. The y axis is energy, and the x axis is a generalized coordinate that describes the coupling of the electronic energies of the defect (red curves) and the lattice. The zero-phonon line (ZPL) energy is labeled, as well as the Frank-Condon relaxation energies in the excited (E_e^{FC}) and ground (E_g^{FC}) electronic state. The inset shows a schematic of a luminescence spectra with the ZPL labeled.

We note that this approach, i.e., relying on cDFT for the excited-state structure, and assuming that $E_g^{\mathrm{FC}} = E_e^{\mathrm{FC}}$, may not be generally applicable, and thus motivates the implementation of forces in the embedding scheme, which will be the topic of future work.

C. Downfolding via Wannierization

The next step of the calculation is to construct the active space and to "downfold" the full electronic structure to the MB Hamiltonian in this subspace. As discussed in Sec. IV A, with the ground-state geometry fixed, we perform a *spinless* DFT calculation. From this we construct the localized basis for the correlated subspace $\phi_i(r)$ via Wannier constructions utilizing the WANNIER90 [90] package. In the cases where the correlated defect states are in the gap, such as C_BC_N and Fe_{Al} we surround them with a "frozen window" so that the single-particle Wannier Hamiltonian defined by the hopping matrix elements

$$t_{ij} = -\langle \phi_i | H_{\mathrm{DFT}} | \phi_j \rangle \tag{3}$$

reproduces the DFT eigenvalues exactly; for states that are resonant with the bulk bands, such as the lower $a_1(1)$ state in NV^-, we rely on initial projections of defect orbitals to disentangle the defect states.

Due to the gauge freedom when constructing Wannier functions, it is crucial to ensure that the specific procedure to generate them does not influence the final results. To test this, we perform calculations of the MB states of C_BC_N with

and without maximally localizing the Wannier functions from their initial projections (on C p_z orbitals). The different choice of Wannier basis does indeed change the values of the hopping and Coulomb matrix elements. However, the final observables such as the resulting MB energies, are the same for the different choices of Wannier functions. This confirms that our final results do not depend on the gauge choice of the initial Wannier basis. For C_BC_N we will use the not-maximally-localized Wannier functions for our subsequent calculations, as it results in a slightly more symmetric basis.

In the case of the NV^- center, the Wannierization procedure is slightly more complicated since, as mentioned above, the $a_1(1)$ state must be disentangled from the valence band manifold. To do this, we chose sp^3 initial projections on the atoms surrounding the vacancy [see Fig. 2(b)], but, unlike for C_BC_N, we maximally localize the Wannier functions. The localization procedure is constrained to exactly reproduce the Kohn-Sham eigenvalues for the $a_1(2)$ and e states in the gap, with a disentanglement window large enough to include the $a_1(1)$ state in the diamond VB. In any case, the relevant MB excited states do not involve significant depopulation of $a_1(1)$, so the specifics of its treatment is not so crucial. We find that this procedure provides us with an accurate basis for subsequent MB calculations.

The situation for Fe_{Al} is similar to C_BC_N in that all of the relevant states are in the band gap [Fig. 3(a)]. Thus, if we begin with d projections on the Fe, there is very little change whether we localize or not. As with C_BC_N, we will not localize in order to preserve the symmetry of the basis.

D. Obtaining the screened interaction parameters

1. Constrained random-phase approximation

The next step is to obtain screened interaction parameters U_{ijkl} in the subspace of defect orbitals. We construct these from the localized Wannier basis via

$$U_{ijkl} = \langle\phi_i\phi_j|\widehat{U}|\phi_k\phi_l\rangle = \iint d^3r\, d^3r'\, \phi_i^*(r)\phi_k(r)\, U(r,r')\, \phi_j^*(r')\phi_l(r') \quad (4)$$

using the partially screened Coulomb interaction in the static limit

$$\widehat{U} = [1 - \hat{v}\,\widehat{\Pi}_{\mathrm{cRPA}}(\omega = 0)]^{-1}\hat{v}. \quad (5)$$

Here $\hat{v}$ is the bare Coulomb interaction and $\widehat{\Pi}_{\mathrm{cRPA}}$ is the partial polarization as defined within the constrained random phase approximation (cRPA) as [58]

$$\widehat{\Pi}_{\mathrm{cRPA}} = \widehat{\Pi}_{\mathrm{full}} - \widehat{\Pi}_{\mathrm{defect}}, \quad (6)$$

where the "full" polarization takes all RPA screening processes from the KS states into account, and the "defect" polarization accounts only for screening processes within the defect-state manifold. In this way U_{ijkl} is screened by the bulk host material; the screening *within* the defect-state manifold is subsequently included exactly via the solution of the Hamiltonian defined in Eq. (2). We perform these cRPA calculations using a recent implementation by Kaltak [91] within VASP. This method requires a mapping between the Wannier and Bloch-band bases to define $\widehat{\Pi}_{\mathrm{defect}}$; this mapping is exact if no disentanglement is necessary, and we find that, in any case, the results are insensitive to the specific method used (i.e., "weighted" [102] versus "projected" [91]).

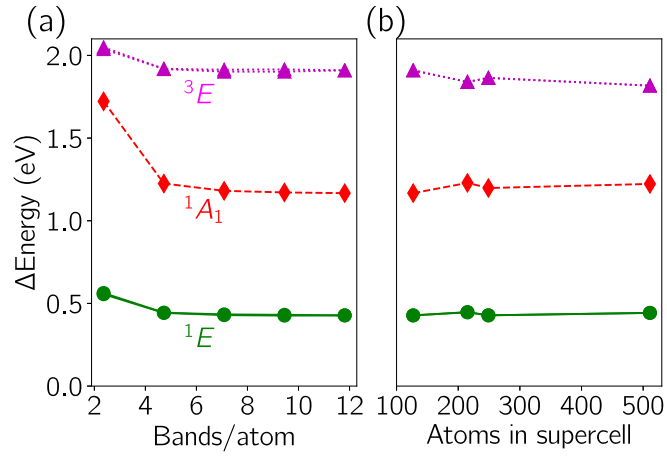

FIG. 5. Convergence of the NV^- energies of many-body states (with respect to the $|^3A_2\rangle$ triplet ground state) with (a) number of bands in the cRPA calculation (for a 127-atom cell), and (b) supercell size (Bands/atom >7 for all cells). The PBE functional is used for the initial DFT calculation, and no double-counting correction is applied.

Finally, we note that RPA and cRPA calculations based on KS-DFT input for gapped systems benefit from an error cancellation initially introduced due to missing higher order diagrams in RPA [103].

2. Convergence of the screened interaction

The convergence of the screening is key to obtaining accurate MB energies, as we will demonstrate for our test-case defects. In the bulk, the screening should be converged with respect to the number of virtual orbitals (in conventional sum-over-states implementations), and k points used to sample the Brillouin zone. For the defective system, increasing the supercell size with a single k point achieves the latter convergence via band folding, while maintaining the zero-dimensional (0D) nature of the calculation (i.e, avoiding contributions from the spurious dispersion of the defect states caused by interactions between periodic images). In Fig. 5, we show that the convergence of the excited-state energies for NV^- (with respect to the $|^3A_2\rangle$ ground state). We see that the main source of convergence is the number of empty bands used in the cRPA calculation; the influence of supercell size is relatively less important. This is a significant result, since it is often found (e.g., Ref. [42]) that large supercells (>500 atoms) are necessary to obtain converged DFT total energies for NV^-; we believe that our localized basis set is the reason for the significantly improved convergence with supercell size.

The convergence in the case of C_BC_N is more complicated. As with NV^-, the MB excitation energies are well-converged for >5 bands per atom in the supercell [Fig. 6(a)]. However, we see from Fig. 6(b) that the convergence with supercell size is difficult to achieve; for the accessible supercell sizes (before we are limited by the computational demand of the cRPA calculation), the MB energies have oscillatory behavior. The reason for this is the slow convergence of the screened

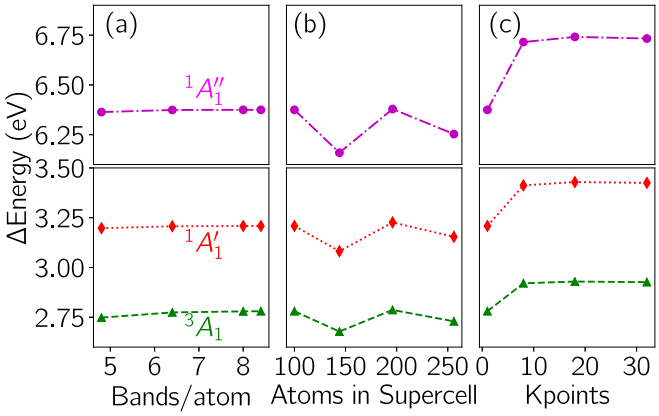

FIG. 6. Convergence of the C_BC_N energies of many-body states (referenced to the ground-state singlet state $|^1A_1\rangle$) of the triplet $|^3A_1\rangle$, first excited singlet $|^1A_1'\rangle$, and second excited state singlet $|^1A_1''\rangle$ with respect to (a) bands/atom (in the 100-atom cell), (b) size of supercell and (c) number of k points (100 atom cell). The PBE functional is used for the initial DFT calculation and no double-counting correction has been applied.

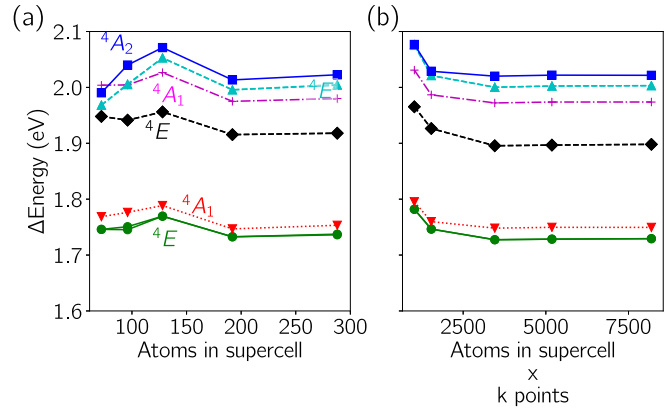

FIG. 8. Convergence of energies of many-body states of Fe_{Al} in wurtzite AlN referenced to the $|^6A_1\rangle$ with (a) number of atoms in the supercell (Bands/atom >11 for all cells); (b) "effective" supercell size, i.e., atoms multiplied by k points; points correspond to a 128-atom and 192-atom cells with a $2 \times 2 \times 2$, $3 \times 3 \times 3$, and $4 \times 4 \times 4$ (only for the 128-atom cell). The PBE functional is used for the initial DFT calculation, and no double-counting correction has been applied.

Coulomb interaction with cell size, as shown via the polarizability [see Eq. (5)] in Fig. 7. We find that a method for accelerating this convergence, is to increase the in-plane k-point mesh, as shown in Fig. 7. We can think of the number of atoms multiplied by the number of in-plane k points as an "effective" supercell size from the point of view of the bulk screening. From Fig. 6(b), the largest supercells we could treat contained 250 atoms, while the screening in this layered compound clearly requires at least double that to converge, likely due to the nonlocal character of the bulk background dielectric function of layered semiconductors [104–106]. In addition, we see from Fig. 7 that the spread of the Wannier functions also converges slowly with cell size. Figure 6(c) shows that indeed, increasing the k mesh allows us to obtain converged energies of the MB states.

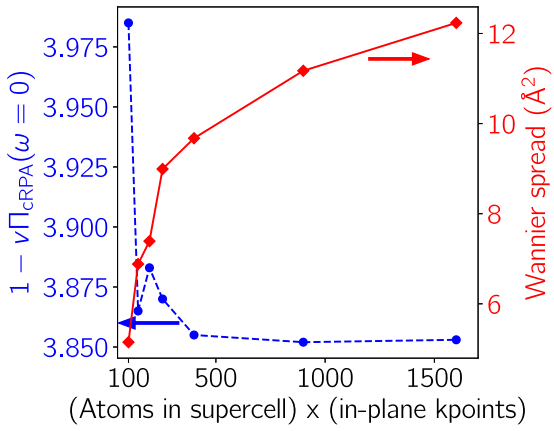

FIG. 7. Convergence of the polarizabilty [see Eq. (5)] and spread of the Wannier functions for C_BC_N with respect to effective atom number, i.e., the number of atoms in the super cell multiplied by the number of k points in plane. Calculations are for projected Wannier functions with C p_z character. The PBE functional is used for the initial DFT calculation.

Using multiple k points means that our Wannier Hamiltonian is no longer strictly 0D, i.e., interdefect hopping is possible, and the spurious dispersion of the defect states is sampled. However, we find that even for the $5 \times 5 \times 1$ cell, the largest intersite hopping element is 0.09 eV [107]. This gives us confidence that we are not affected by the spurious dispersion caused by interactions between the defect and its periodic images.

We find in the case of C_BC_N that the out-of-plane k mesh and supercell size has a relatively small (see Sec. S1A of the SM [61]) effect on the screening of the MB states, which is due to the quasi-2D nature of the host material BN. However, we can use the same procedure for a 3D material, but increasing the k mesh in all three dimensions. We demonstrate this for our remaining test case, Fe_{Al}, in Fig. 8. In panel (a) we show the convergence of the energies of excited MB states with respect to supercell size. Though the convergence can be achieved, a cell of around 200 atoms is required for quantitative accuracy. In Fig. 8(b) we show this convergence versus "effective" supercell size, i.e., the number of atoms multiplied by the number of k points (in all directions this time since our system is 3D). The points at large effective size correspond to 128-atom and 192-atom cells with a $2 \times 2 \times 2$, $3 \times 3 \times 3$, and $4 \times 4 \times 4$ (only for the 128-atom cell) k meshes. As we can see the MB energies converge smoothly, agreeing with the results from larger actual supercells. The largest hopping between the defect and its periodic images was less than 0.006 eV, indicating that we have preserved the 0D nature of our noninteracting Wannier Hamiltonian.

E. Choice of DFT functional for initial calculation

We now return to another crucial element relating to the initial DFT calculation, how the the choice of XC functional influences the MB Hamiltonian, and ultimately the energies of MB states. To explore this, we compare results with the DFT calculation performed with the HSE hybrid functional

[94,95], which has become the standard for quantitative calculations of defect properties [15], to the results with PBE [97], which is one of the most popular functionals for solid-state applications. We analyze the effect of XC functional on the calculation of t_{ij}, which encapsulates the information about the single-particle energies, as well as the Coulomb interactions U_{ijkl}, which may also differ for different functionals. In order to discuss the interactions, we will compare orbitally-averaged values between functionals, i.e., $U = \frac{1}{N_{\text{orb}}} \sum_i U_{iiii}$ (intraorbital density-density interaction, N_{orb} is the number of orbitals), $U' = \frac{1}{N_{\text{orb}}(N_{\text{orb}}-1)} \sum_{i \neq j} U_{ijij}$ (interorbital density-density interaction), and $J = \frac{1}{N_{\text{orb}}(N_{\text{orb}}-1)} \sum_{i \neq j} U_{ijji}$ (Hund's exchange coupling). These values incorporate much of the physics of the Coulomb interaction in atomic-like systems (see Sec. V B).

Note that there is a crucial interplay between XC functional for the initial DFT calculation and the double-counting correction used. This will be discussed in Sec. IV F.

A key question regarding the use of hybrids like HSE is the choice of mixing parameter α, since gaps between single-particle levels (e.g., the band gap of the host material) scales with α. In many cases, α is chosen to roughly reproduce the experimental band gap of the material, though there are also *ab initio* approaches to determining the mixing [108]. In this paper, we will rely on the values shown to produce accurate results in previous computational studies. We will show in Sec. IV F that an appropriate double-counting correction for hybrids should include α, and thus should remove much of the dependence of the MB energies on the starting XC functional.

For the case of C_BC_N, we tune the mixing parameter of the HSE functional to $\alpha = 0.4$, as was done in Ref. [65]. The main quantitative effect of HSE is on the single-particle states. Firstly, the eigenvalue difference between the C-derived states increases by a factor of 1.5 (from 3.45 eV with PBE to 5.25 eV with HSE), as does the band gap (4.54 eV to 6.85 eV). Though the Wannier-function spread is slightly reduced with HSE, which results in a slightly larger unscreened Coulomb interaction, the main effect on the U_{ijkl} elements is due to the reduced environmental screening (due to the larger gaps between single-particle states, both bulk-bulk and bulk-defect). This results in a significant increase in the screened Coulomb matrix elements, e.g., of more than 500 meV for the density-density terms (i.e., those where $i = j, k = l$). If we perform an average over the orbitals in the Wannier basis (see Sec. V B), we obtain intraorbital $U = 2.73$ eV, interorbital $U' = 1.90$ eV, and Hund's coupling $J = 0.09$ eV. Compared to the values we calculated for PBE ($U = 1.94$ eV, $U' = 1.41$ eV, and $J = 0.08$), the most significant change is an increase in the intraorbital U.

For the MB states of C_BC_N, the effect of HSE for the initial DFT calculation is manifested as an increase in energy between $|^1A_1\rangle$ and the excited state singlet $|^1A_1'\rangle$ of 1.62 eV. The splitting between $|^3A_1\rangle$ and $|^1A_1'\rangle$ only increases by 0.12 eV, as it depends on the exchange interaction and not the splitting of the single-particle levels. The $|^1A_1\rangle$ to $|^1A_1''\rangle$ splitting is increased by 3.26 eV, or approximately twice the increase in $|^1A_1\rangle$ to $|^1A_1'\rangle$, due to the fact that $|^1A_1''\rangle$ involves two electrons in the antibonding orbital. See the "No DC" points on Figs. 9(a) and 9(b) for a comparison of the energies calculated with HSE and PBE for the initial DFT.

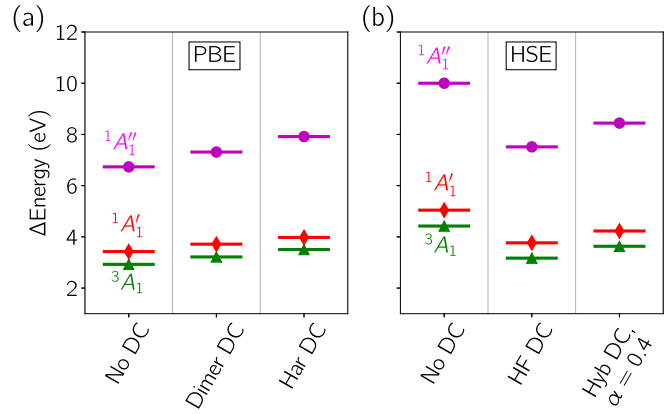

FIG. 9. Excited state energies of C_BC_N many-body states in BN with respect the ground-state singlet $|^1A_1\rangle$ calculated with either (a) PBE or (b) HSE used for the initial DFT calculation, with and without double-counting (DC) corrections (described in Sec. IV F).

Compared to the ΔSCF HSE calculations of Ref. [65], the singlet-singlet splitting ($|^1A_1\rangle$ to $|^1A_1'\rangle$) energies that we obtain are about 500 meV larger; e.g., the ZPL that we find is 4.86 eV versus 4.31 eV in Ref. [65] [c.f., "No DC" in Fig. 10(b)]. The reason for this overestimation is at least partially due to the fact that, as discussed in Sec. III, the original DFT calculation includes some approximate Coulomb interaction, the effect of which should be removed with the DC correction (discussed in the next section). Hybrid functionals often have a similar effect on the electronic structure in terms of improving the description of localized states as, e.g., DFT + U, and thus we expect that they contain more of the Coulomb interaction than local and semilocal functionals.

The HSE functional has been used in the past to obtain optical properties of NV^- in excellent agreement with experiment [3,101,109]. The main effect of the HSE ($\alpha = 0.25$) functional for NV^- (similar to C_BC_N), is to increase the splitting between the $a_1(2)$ and e levels (2.14 eV for HSE versus 1.50 eV for PBE). This results in a significantly increased splitting between the ground-state triplet $|^3A_2\rangle$ and the

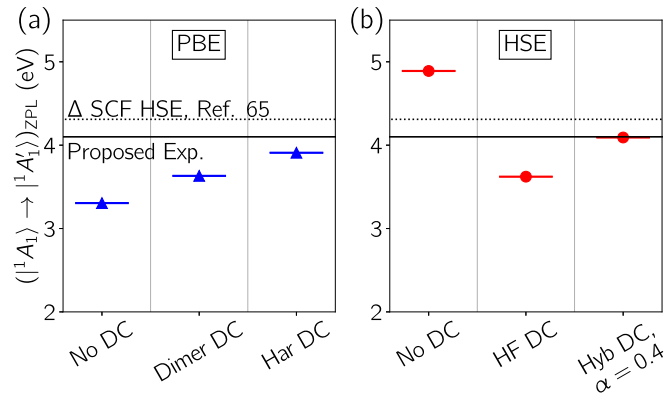

FIG. 10. $|^1A_1\rangle \rightarrow |^1A_1'\rangle$ zero-phonon line energy from many-body states of C_BC_N in BN calculated using either (a) PBE or (b) HSE for the initial DFT calculation, with and without double-counting (DC) corrections (described in Sec. IV F). Proposed experimental attribution and ΔSCF HSE from Ref. [65].

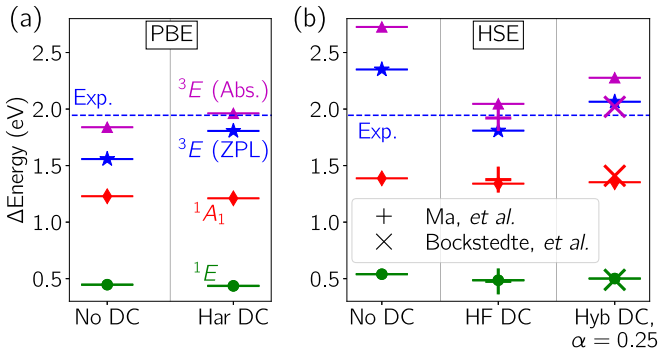

FIG. 11. Energies of many-body excited states of NV^-, and zero-phonon-line energy for the $|^3A_2\rangle \rightarrow |^3E\rangle$ transition (blue stars, experimental value is blue dashed line) calculated with either (a) PBE or (b) HSE for the initial DFT calculation, with and without double-counting (DC) corrections (described in Sec. IV F). Previous results are included from Ma *et al.* (Ref. [41]) and Bockstedte *et al.* (Ref. [42]).

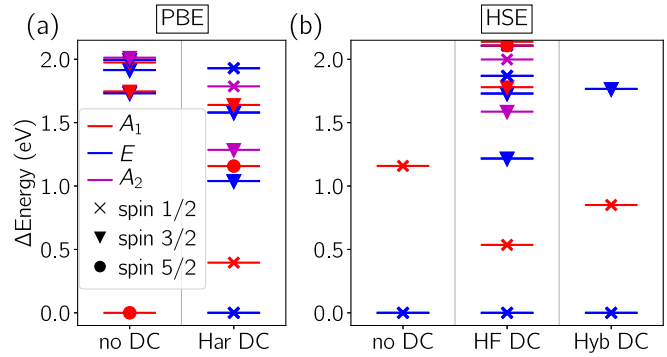

FIG. 12. Energies of many-body ground and excited states of Fe_{Al}, referenced to the lowest energy state, calculated with (a) PBE or (b) HSE for the initial DFT calculation, with and without double-counting (DC) corrections (described in Sec. IV F).

excited-state triplet $|^3E\rangle$ MB states (2.73 eV vertical excitation when HSE is used for the initial DFT calculation versus 1.84 when PBE is used, see "No DC" points in Fig. 11), as well as, to a lesser extent, $|^1A_1\rangle$ (1.39 eV vertical excitation when HSE is used for the initial DFT calculation versus 1.22 eV when PBE is used); both $|^3E\rangle$ and $|^1A_1\rangle$ involve exciting an electron from the a_1 to the e state. The energy of the $|^1E\rangle$ MB state changes less between PBE and HSE starting points (0.54 eV vertical excitation using HSE for the initial DFT calculation versus 0.45 eV for PBE), as it is not directly influenced by the splitting of single-particle states. Comparing the cRPA Coulomb tensors, the main difference between the PBE and HSE starting point is that HSE has a slightly larger intraorbital screened interaction (averaged parameters for HSE: $U = 2.83$ eV, $U' = 0.98$, $J = 0.02$ versus $U = 2.43$ eV, $U' = 0.81$ eV, and $J = 0.03$ eV for PBE, see Sec. V B). This is a result of the decreased environmental screening due to the larger band gap in HSE.

Thus, from the examples of C_BC_N and NV^-, we would conclude that HSE provides a better description of the initial single-particle electronic structure (e.g., bulk band gaps and splitting of single particle levels), and thus is a good starting point for our embedding methodology. However, the case of Fe_{Al} is significantly more complicated. The reason for this, as pointed out above, is that HSE includes additional aspects of the interaction (i.e., exact exchange) in the part of the Hamiltonian that is intended to be noninteracting.

For HSE, the splitting between the a_1 and e states by the C_{3v} crystal field (i.e., the states that are originally degenerate with t_2 symmetry in T_d) is very large (>1.5 eV), with a_1 lower in energy; there is also a significant splitting in the higher-energy e single particle levels of 200 meV in spite of the fact that the calculation has C_{3v} symmetry, see Fig. S2(c) in SM [61]. If we constrain the electronic structure to look more like that calculated with PBE, i.e., forcing the e states to be half filled, we recover the degeneracy of the e state by construction, Fig. S2(d) in SM [61]. The a_1 state is now *higher* in energy by 900 meV, compared to 20 meV for PBE. This difference cannot be attributed to structural differences between HSE and PBE; performing a PBE calculation with the HSE structure gives electronic states that are close to the PBE calculation in its own ground-state structure (i.e., the crystal field splitting of the t_2 state into a_1 and e is 30 meV).

The large single-particle energy splittings in the ground state for HSE results in MB states that significantly differ from those using PBE for the initial DFT calculation, experimental observations [78–80], and spinful DFT calculations [76] (see also Sec. S2C2 of the SM [61]). Specifically, the ground state is low spin ($S = 1/2$), as predicted [77] for large CFS, as opposed to the high spin $S = 5/2$ as expected [76,78–80] (see "No DC" points on Fig. 12). Thus, even though HSE clearly provides a better description of the bulk electronic structure and screening in AlN (and the other host materials discussed in this paper), it appears problematic in Fe_{Al} for a noninteracting starting point of the correlated subspace. We will extend on this discussion after introducing the DC correction in the next section.

F. Double-counting correction

In the previous sections, we discussed how we obtain the single particle and the screened interaction matrix elements in the correlated subspace as needed for the Hamiltonian in Eq. (2). In principle, however, the separation of the noninteracting part from the Coulomb interactions has fundamental incompatibilities with DFT calculations. This is because the DFT calculation already includes Coulomb interactions within the correlated subspace in an approximate way, which does not have a rigorous definition within MB perturbation theory [38,60]. This issue is usually dealt with by applying a "double-counting" (DC) correction to the hopping matrix elements.

Within the DFT-based embedding community (e.g., DFT + U and DFT + DMFT), the most common approaches apply a DC correction potential that involves orbitally-averaged interaction parameters U and J, and moreover assumes no orbital polarization, i.e., that the orbital levels are degenerate [60,110]. Such a DC correction will shift the correlated subspace with respect to the uncorrelated states, and possibly alter the total occupation, but will not change the energy splitting between orbitals in the correlated subspace,

which is our focus. Also, in our approach, the occupation is enforced in all cases in the MB calculation via the chemical potential μ in Eq. (2). Thus a fully orbitally-averaged DC correction will have no effect on the results.

It has been found before [42,43,111,112] and is confirmed in our results below that an *orbitally selective* version of the DC correction is required to obtain agreement with experiment. However, there is vanishingly little work on benchmarking such an approach in general, and systematic investigations of the DC for defect embedding methodologies are not yet available.

1. Form of the orbitally-resolved double-counting correction

A systematic methodology for obtaining an orbitally-resolved DC correction for extended systems was given in Ref. [60], and we will center our discussion around that approach. The general idea is to determine the DFT treatment of the Coulomb interaction in the subspace by making equivalent DFT approximations within that space. Thus, the charge density distribution is constructed from our Wannierized defect states, as opposed to the KS bands of the entire system. Also, the Coulomb interactions that enter the Hartree term, and are used to construct the XC, should be the screened interaction determined by cRPA (see Sec. IV D).

The Hartree contribution to the Coulomb interaction in the subspace is easy to calculate in our basis, and can be written as [42,43,113]

$$H_{\mathrm{DC}}^{\mathrm{Har}} = \sum_{ij,\sigma} c_{i\sigma}^{\dagger} c_{j\sigma} \sum_{kl} \rho_{kl} U_{iljk}, \tag{7}$$

where ρ_{kl} is the component of the single-particle occupation matrix for (Wannier) orbitals k and l and U_{iljk} is the density-density screened Coulomb interaction in our subspace; since our calculation is spinless, ρ_{kl} ranges over the number of orbitals with a maximum occupancy of two electrons per orbital [113]. The XC term is more complicated to obtain [60]; for, e.g., DFT under the local density approximation (LDA), it would require calculating the density-dependent XC energy of the uniform electron gas, using the screened interaction given by Eq. (5). An important point to note is that such a potential would be calculated from the *total orbital averaged density* in the active space, as opposed to the Hartree term in Eq. (7), which is obtained from the *orbitally specific* density-density interaction. Thus the XC part is expected to have a weaker contribution to relative shifts of orbitals within the active space than the Hartree term, although it will still have some influence since the different orbitals have different spatial distributions of charge densities. In this study, we will neglect this term, as was done in Ref. [42]. It is important to note that if we were interested in the alignment between the defect states of our correlated subspace and the bulk states, the XC contribution must be included for a consistent DC scheme.

In the case where we are using a hybrid functional, we will have an additional orbital dependence arising from the Fock exact-exchange operator. For a full Hartree-Fock calculation, the Coulomb interaction, and thus the DC correction that should be subtracted in the MB Hamiltonian is [42,43,113]:

$$H_{\mathrm{DC}}^{\mathrm{HF}} = \sum_{ij,\sigma} c_{i\sigma}^{\dagger} c_{j\sigma} \sum_{kl} \rho_{kl} \left(U_{iljk} - \frac{1}{2} U_{ilkj} \right). \tag{8}$$

This was used as the DC correction in Refs. [43,44,114]. From Eqs. (7) and (8), we see that a logical form of the DC correction for hybrid functionals is [42]:

$$H_{\mathrm{DC}}^{\mathrm{hyb}} = \sum_{ij,\sigma} c_{i\sigma}^{\dagger} c_{j\sigma} \sum_{kl} \rho_{kl} (U_{iljk} - \alpha U_{ilkj}), \tag{9}$$

where α is the mixing parameter of exact exchange in the hybrid functional. We will explore these forms of the DC in the next section.

2. Effect of double-counting correction on many-body energies

We will now discuss the orbitally-resolved DC corrections introduced in the previous section in the context of our test-case defects, starting with $C_B C_N$. Because of the simplicity of the defect electronic structure, the DC correction is particularly simple to interpret in this case. In addition, the correspondence with the dimer model (see Sec. S2A1 of the SM [61]) allows the calculation of a "dimer" DC that takes into account specifically the Coulomb interactions included in Kohn-Sham DFT [103,115] for a system with a single filled valence orbital and empty conduction orbital [see Fig. 1(a)]. Note that, in principle, this DC correction is constructed for the exact XC functional [103]. A discussion of this form of the DC is given in Sec. S2A2 of the SM [61].

Figure 9 shows the effect of the DC correction on the MB excitation energies for $C_B C_N$. The levels on the left of each panel are calculated with no DC correction. For the calculations starting from PBE [Fig. 9(a)], we use the dimer DC (Sec. S2A2 of the SM [61]), and the approach of removing just the Hartree term [Eq. (7)]. In both cases, the main result of the DC correction is to increase the splitting between the b_2 and b_2^* single-particle states; since all MB excited states involve electron(s) being promoted from b_2 to b_2^*, the MB energies are shifted up with respect to the ground state. The dimer DC involves an explicit shift of the levels (i.e., it is diagonal in the band basis by construction) of $\Delta\epsilon^{\mathrm{DFT}} = U_{b_2 b_2 b_2 b_2} - U_{b_2^* b_2 b_2^* b_2}$ (Sec. S2A2 of the SM [61]). Since the intraorbital interaction is slightly larger than the interorbital one, the DC correction slightly increases the splitting between the single particle states. For $H_{\mathrm{DC}}^{\mathrm{Har}}$ ("Har DC" on Fig. 9), the only nonzero element of the occupation matrix is $\rho_{b_2 b_2} = 2$, so the DC correction shifts down the b_2 level, increasing the gap to b_2^* (the shift is slightly larger than for the dimer DC due to small nonzero terms in the interaction in addition to the strict density-density $U_{b_2 b_2 b_2 b_2}$ and $U_{b_2^* b_2 b_2^* b_2}$).

In Fig. 9(b) we compare the effect of the DC correction [full Hartree-Fock DC Eq. (8) and the hybrid version Eq. (9)] on the MB energies using the HSE functional for the initial DFT calculations. We see that the DC has the opposite effect, the energies of the excited states are *reduced* compared to the ground state. This is a direct result of the inclusion of exact exchange in the DC, which reduces the splitting between the single-particle defect levels. In the band basis, for the Hartee-Fock DC, this change in splitting is given by $\Delta\epsilon_{\mathrm{DC}} = U_{b_2 b_2 b_2 b_2} - 2U_{b_2^* b_2 b_2^* b_2} + U_{b_2^* b_2 b_2 b_2^*}$. We

find that, in our calculations, $U_{b_2b_2b_2b_2} \simeq U_{b_2^*b_2b_2^*b_2} \gg U_{b_2^*b_2b_2b_2^*}$ (e.g., for HSE: $U_{b_2b_2b_2b_2} = 2.096$ eV, $U_{b_2^*b_2b_2^*b_2} = 2.099$ eV, $U_{b_2^*b_2b_2b_2^*} = 0.311$ eV). Therefore $\Delta\epsilon_{\mathrm{DC}} < 0$. In the $H_{\mathrm{DC}}^{\mathrm{Hyb}}$ case, this decrease is reduced due to the mixing parameter.

In Fig. 10, we show the effect of the DC correction on the lowest-energy singlet-singlet ZPL (see Sec. IV B) for C_BC_N. We see that, in both cases, the DC improves the agreement with the ΔSCF results of Ref. [65], and thus the proposed experimental attribution (see Sec. S2A3 of the SM [61] for full comparison with ΔSCF calculations of Ref. [65]).

We also note that using an appropriate DC correction, i.e., "dimer" or "Har" for the PBE DFT starting point and "Hyb" for calculations using HSE starting point, significantly reduces the dependence of the final results (in terms of MB energies and ZPL) on the XC functional used for the initial DFT calculation. As this was the intended effect of the DC correction, these results are quite promising.

We see a similar effect for NV^- in diamond (Fig. 11), where the energies of the MB excited states are increased in the case of the PBE starting point, and decreased for HSE. As with C_BC_N, the main effect of the DC is to shift the single-particle energies. Thus the $|^3E\rangle$ energy changes the most, since it involves promotion of an electron from $a_1(2)$ to e. The DC brings the triplet-triplet ZPL (blue stars in Fig. 11) in better agreement with the experimental value (dashed line in Fig. 11). Note that ΔSCF calculations for the triplet-triplet ZPL are also in good agreement with experiment, see Sec. S2B1 of the SM [61] for a detailed comparison.

In addition, we can see that our results match well with the previous implementation of the embedding methods (Ref. [43] used the HF DC scheme, and Ref. [42] used the hybrid DC), indicating that the general methodology is relatively robust to the details of the calculations, e.g., DFT codes, cRPA implementation, basis, etc. We note that Ma *et al.* [43] (who used the HF DC scheme) also used a "beyond RPA" strategy which includes the influence of exchange-correlation on the screening, which found a significantly higher value for the energy of $|^1A_1\rangle$, 1.759 eV compared to 1.376 eV for standard cRPA [standard cRPA is plotted with the red crosses in Fig. 11(b)].

The situation for Fe_{Al} in AlN is significantly more complicated. For NV^- and C_BC_N, the DC correction simply renormalized the energy splittings of the excited MB states, via changing the splittings of the single-particle levels. For Fe_{Al}, the nature of the MB ground and low-lying excited states depends sensitively on the splitting of the single particle levels (i.e., the CFS between the e and t_2 Fe $3d$ states, as discussed in Sec. II C). This is known from ligand-field theory, where the d^5 Tanabe-Sugano diagram predicts a high-spin $^6A_1$ ground state for small CFS and a low-spin $^2T_2$ for large CFS [77] since the latter involves a smaller occupation of t_2 single-particle states.

In Fig. 12(a), we show the ground and excited states calculated from a PBE starting point, with and without the Hartree term of the DC [Eq. (7)]. As discussed above, without DC, the ground state starting from PBE is a sixfold degenerate spin 5/2 state with A_1 orbital symmetry. The excited states are split from the spin 3/2 ^4G manifold of the free atom by the crystal field. When we add the DC correction, however, the low-spin state is favored; the symmetry lowering from the cubic T_d crystal field to the C_{3v} hexagonal one splits the spin 1/2 $|^2T_2\rangle$ state into $|^2E\rangle$ and $|^2A_1\rangle$ states. For the low-lying excited states, there is a mixture of spin 1/2 states originating from the ^2I manifold of the free atom, and the spin 3/2 states from ^4G. Also we see the $|^6A_1\rangle$ state has now moved over 1 eV above the ground state.

In Fig. 12(b) we plot the energies of the MB states using an HSE starting point. (As discussed above, the occupation was constrained to be the same as the PBE calculation, see Sec. S2C1 of the SM [61].) We can see that, similar to the PBE calculation with DC correction, the low-spin state is the ground state, and the splitting of the $|^2T_2\rangle$ state from the C_{3v} crystal field is very large. Thus, the other excited states are much higher in energy. Including the HF or hybrid DC correction reduces the splitting somewhat, but it is still much larger than the case of PBE, and the ground state is still $S = 1/2$.

As discussed above in Sec. II C, it is expected that the ground state of Fe_{Al} should be the high spin $|^6A_1\rangle$ state (see Sec. S2C2 of the SM [61]). We see in Fig. 12 that the PBE starting point with no DC correction is the only case that correctly reproduces this ground state, as well as the expected low-energy excited states (Sec. II C and Fig. S1 in the SM [61]). As was the case for NV^- and C_BC_N, the Hartree DC correction tends to increase the splitting between the single-particle energies, which for Fe_{Al} favors the low-spin ground state. We therefore conclude that, in this case, the Hartree DC correction is *overcompensating* for the Coulomb interaction included in the initial PBE DFT calculation. For the case of the HSE starting point, it seems that the DC correction does not provide *enough* compensation to undo the significant overestimation of the single particle splittings, both between the e and t_2 manifold, and within t_2 from the C_{3v} crystal field. In both cases, it is possible that including the semilocal XC contribution to the DC (see Sec. IV F 1) will mitigate this overcompensation, motivating the development of the full treatment advocated in Ref. [60]. In any case, for our current capabilities, Fe_{Al} represents a failure of the DC approaches described in this section, and provides a stringent test case for further development of the DC, and the embedding approach as a whole.

V. DISCUSSION

A. Multireference nature of the many-body states

A key utility of embedding methods such as the one described in this paper is that they can treat "multireference" states, which cannot be described by a single Slater determinant; this goes beyond the capability of, e.g., DFT or Hartree-Fock theory. Therefore, for understanding the efficacy of the method in going beyond the traditional single-particle theories, it is important to have a metric to understand the degree of multireference nature of the states that we are dealing with. In principle, this can be obtained by analyzing the MB wavefunctions themselves, but care must be taken to differentiate states that are fundamentally multireference, i.e., cannot be expressed as a single Slater determinant in *any basis*, and those that appear multireference because they are a sum of several Fock states in our chosen basis.

To accomplish this, we focus on the one-particle density matrix, $\widetilde{\rho}_{i\sigma\, j\sigma'} = \langle\Psi|c^{\dagger}_{i\sigma}c_{j\sigma'}|\Psi\rangle$, where Ψ is a MB state. Then, the MB state can be written as a single Fock state if and only if the density matrix is idempotent, i.e., $\widetilde{\boldsymbol{\rho}} = \widetilde{\boldsymbol{\rho}}^2$ [116]. To probe this property, we define the quantity

$$\Lambda_{\rm MR} = {\rm Tr}(\widetilde{\boldsymbol{\rho}} - \widetilde{\boldsymbol{\rho}}^2) = {\rm Tr}(\widetilde{\boldsymbol{\rho}}) - {\rm Tr}(\widetilde{\boldsymbol{\rho}}^2). \tag{10}$$

Note that $\Lambda_{\rm MR}$ is basis independent due to the cyclic property of the trace. For a state that can be described as a single Slater determinant in some basis, $\Lambda_{\rm MR} = 0$. The maximum value will depend on the number of electrons $N_{\rm el}$ available to fill the $2N_{\rm orb}$ states (the factor of 2 is for spin). Without loss of generality, we choose a basis where $\widetilde{\boldsymbol{\rho}}$ is diagonal, so that

$$\Lambda^{\rm diag}_{\rm MR} = \sum_{i=1}^{2N_{\rm orb}} \left(\widetilde{\rho}_{ii} - \widetilde{\rho}^2_{ii}\right), \tag{11}$$

subject to the constraint, $\sum_{i=1}^{2N_{\rm orb}} \widetilde{\rho}_{ii} = N_{\rm el}$. Then $\Lambda^{\rm diag}_{\rm MR}$ in Eq. (11) is maximized when $\widetilde{\rho}_{ii} = N_{\rm el}/2N_{\rm orb}$. It follows that

$$\Lambda^{\rm max}_{\rm MR} = N_{\rm el} - 2N_{\rm orb}\left(\frac{N_{\rm el}}{2N_{\rm orb}}\right)^2 = N_{\rm el} - \frac{N^2_{\rm el}}{2N_{\rm orb}}. \tag{12}$$

Notice that when $\Lambda_{\rm MR}$ reaches its maximum value, $\boldsymbol{\rho}$ is proportional to the identity matrix and thus is basis independent.

As an example, we consider the MB states of C_BC_N given in Table SI (orbital basis) and Table SII (band basis) in the SM [61]. First we see that, as expected, $\Lambda_{\rm MR}$ is basis independent. Beginning with the ground-state singlet $|^1A_1\rangle$, we find $\Lambda_{\rm MR} = 0.006$. Since $|^1A_1\rangle$ is a multiorbital singlet that is expected to be multireference [19,20], $\Lambda_{\rm MR}$ should be finite; however its small value suggests that there is a basis where only one Fock state has the majority of the weight. Indeed, this is the case for the band basis (Table SII in the SM [61]), where the Fock state with two electrons in the bonding state ($|10;10\rangle$) has the vast majority of the weight. For the triplet $|^3A_1\rangle$, the first two MB states (corresponding to $m_s = \pm 1$) are comprised of single Fock states in both bases. Thus $\Lambda_{\rm MR} = 0$, as expected. The third triplet state ($m_s = 0$) is "maximally entangled," i.e., $\Lambda_{\rm MR} = \Lambda^{\rm max}_{\rm MR} = 1$. Thus, in both bases, the MB state for $|^3A_1\rangle$ with $m_s = 0$ involves two Fock states of equal weight. The first excited state singlet $|^1A'_1\rangle$, in contrast with $|^1A_1\rangle$, has $\Lambda_{\rm MR} = 0.991$, close to maximally entangled between two states. In the orbital basis, the state is not qualitatively distinguishable from $|^1A_1\rangle$, however in the band basis we see that, like $|^3A_1\rangle$ with $m_s = 0$, the MB state involves a nearly equal superposition of two Fock states. Finally, the second excited singlet $|^1A''_1\rangle$ has $\Lambda_{\rm MR} = 0.005$ similar to $|^1A_1\rangle$, consistent with the single Fock state with majority weight in the band basis (Table SII in the SM [61]). This analysis of C_BC_N is a clear demonstration of the utility of $\Lambda_{\rm MR}$. We are able to differentiate between the multideterminant nature of the singlet states, which in certain bases is not *a priori* obvious.

An analysis of $\Lambda_{\rm MR}$ for NV^- bears out what is known about the multireference nature of its MB states. We see in Table SIII in the SM [61] that, for the orbital basis, *all* of the states are made up of multiple Fock states. However, for the triplets, there are two states (four for the excited state due to the orbital degeneracy) with $\Lambda_{\rm MR} = 0$, indicating that they *could* be represented by a single Fock state, for a particular choice of basis (as in, e.g., Ref. [71]). For the $|^3A_2\rangle$ state, the band basis in Table SIV in the SM [61] results in single determinant states. However, in either basis, the excited-state $|^3E\rangle$ manifold includes mixtures of different Fock states. The singlets all have $\Lambda_{\rm MR} \simeq 1$. This does not represent maximal entanglement, since for NV^- we have eight total spin-orbitals and six electrons so $\Lambda^{\rm max}_{\rm MR} = 1.5$. Thus the singlets and $m_s = 0$ triplet states are not maximally entangled in the context of our full Hilbert space. However, they are maximally entangled with respect to a smaller Hilbert space; the NV^- MB states primarily involve Fock states with two of the orbitals completely filled by two electrons, and the other two half filled with one spin. This is most clearly seen in the $m_s = 0$ state of $|^3A_2\rangle$ in the band basis (second row of Table SIV in the SM [61], where the Fock states have fully occupied $a_1(1)$ and $a_1(2)$ states, and half occupied e states. Thus the entanglement occurs between four spin-orbitals occupied by two electrons; analogous to the case of C_BC_N, $\Lambda^{\rm max}_{\rm MR}$ for this reduced space is unity.

For the case of Fe_{Al}, the only single-determinant states we find is the $m_s = \pm 5/2$ states of the high-spin $|^6A_1\rangle$ manifold. All other states have $\Lambda_{\rm MR} > 1$, and many of them (Table SV in the SM [61]) are close to maximally entangled, i.e., $\Lambda_{\rm MR} \simeq \Lambda^{\rm max}_{\rm MR} = 2.5$.

B. Obtaining simplified models for defect interactions

In general, the Coulomb interaction is represented by the full four-index U_{ijkl} tensor. Given the minimal basis sets we use for the description of the embedded correlated states, we aim in the following to minimize the number of needed parameters *even further*, by neglecting more and more channels of the full Coulomb interaction tensor. Indeed, in an atomic-orbital picture, the type of orbitals and the point symmetry govern which elements of U_{ijkl} are present; thus by comparing the results from our Wannier basis with those expected assuming atomic-like orbitals, we can gain insight into the interaction between the defect states, and with the bulk. Also, simplified interactions are useful for creating minimal models for further analysis, and may be required for the use of some MB solvers.

We will consider reducing U_{ijkl} to a two-index tensor, where U_{ij} includes the intra- and interorbital density-density interactions ($k = i$ and $l = j$) and J_{ij} includes the Hunds couplings ($i = l$ and $k = j$). Also, we will consider using just three average parameters, U, U', and J (defined in Sec. IV E) to construct the interaction. We will keep the full noninteracting part of Eq. (2) from our Wannier calculations; in this section, we will focus on calculations based on PBE and, to simplify the discussion, neglect the DC correction.

In Fig. 13 we plot the energies of the MB states for C_BC_N with respect to $|^1A_1\rangle$ using these simplified screened Coulomb interaction tensors. Recall that when we solve the Hamiltonian in Eq. (2) including all terms in U_{ijkl}, the orbital and band bases are related by a unitary transformation, and thus result in the same MB energies; however, once we start simplifying the interaction (i.e., removing or averaging terms), the resulting MB energies will depend on which basis for U_{ijkl} that we start from. Thus we plot the energies with simplified

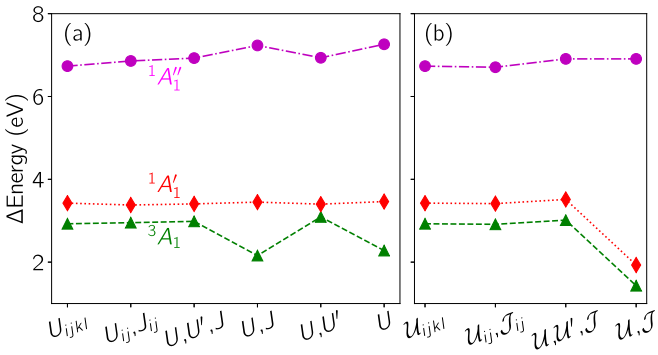

FIG. 13. Energy of the many-body states of C_BC_N in BN, calculated with PBE and no double-counting correction, with respect to the ground-state singlet state for different simplified interactions (see Sec. V B), where orbital averaging is performed using the interaction in the (a) orbital, or (b) band basis. The x labels denote: U_{ijkl}: full interaction tensor; U_{ij}, J_{ij}: two component interactions; U, U', J: orbitally averaged intraorbital and interorbital density-density and Hunds exchange interactions; U, J: orbitally averaged intraorbital density-density and Hunds interactions; U, U': orbitally averaged intraorbital and interorbital density-density interactions; U: orbitally averaged intraorbital interactions. Script versions in (b) correspond to the same quantities, but averaged in the band basis.

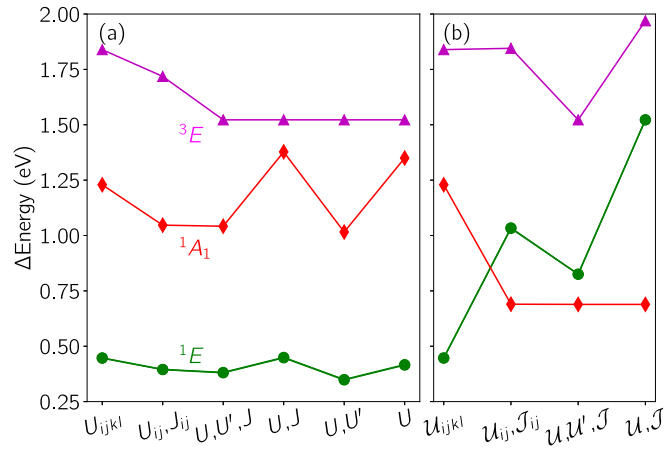

FIG. 14. Energies of the many-body states of NV^- in diamond calculated using the PBE functional for the DFT starting point (no double-counting corrections), with respect the ground-state triplet for different simplified interactions (see Sec. V B), where orbital averaging is performed using the interaction in the (a) orbital, or (b) band basis. The x labels denote: U_{ijkl}: full interaction tensor; U_{ij}, J_{ij}: two component interactions; U, U', J: orbitally averaged intraorbital and interorbital density-density and Hunds exchange interactions; U, J: orbitally averaged intraorbital density-density and Hunds interactions; U, U': orbitally averaged intraorbital and interorbital density-density interactions; U: orbitally averaged intraorbital interactions. Script versions in (b) correspond to the same quantities, but averaged in the band basis.

interactions starting from both the orbital [Fig. 13(a)] and band [Fig. 13(b)] bases (script letters will denote averaging in the band basis).

As discussed in Sec. S2A1 of the SM [61], the energies of the states of C_BC_N can be estimated with just one interaction parameter U, though we construct this value from the difference between the intraorbital and interorbital density-density interaction terms. Simplifying U_{ijkl} to a two-component form does not result in a significant change in the MB spectrum for either basis; e.g., for the orbital basis in Fig. 13(a) all the excited states shifted up in energy by less than 125 meV. Performing an average over the orbitals *in the orbital basis* provides effective parameters, U, U', and J (values reported in Sec. IV E). Taking these orbitally averaged values as the Coulomb interaction only results in changes in the energy at the meV level. Neglecting the Hunds J has a minor effect on the splitting of the spin states, shifting the triplet upward in energy (i.e., closer to the corresponding singlet $|^1A_1'\rangle$) by 166 meV. Both the intraorbital (U) and interorbital (U') terms are necessary for obtaining accurate energies for the triplet state [see Fig. 13(a)].

Performing the averaging in the band basis, we obtain $\mathcal{U} = 1.77$ eV, $\mathcal{U}' = 1.58$ eV, and $\mathcal{J} = 0.25$ eV. The significantly larger value of $\mathcal{J}$ compared to the orbital basis is indicative of the importance of exchange in this basis: neglecting $\mathcal{J}$ does not produce the correct spin states [and thus these points are not included in Fig. 13(b)]. Specifically, $\mathcal{J}$ is necessary to capture the $m_s = 0$ triplet state (otherwise it becomes a spin 1/2 doublet). In the band basis we also see in Fig. 13(b) that both intraorbital and interorbital density-density interactions are required to accurately capture the energies of $|^3A_1\rangle$ and $|^1A_1'\rangle$.

Though the NV^- center has a more complex electronic structure than C_BC_N, we can still hope to gain insight into the MB states and the possibility for simplified models via exploring reduced forms of the Coulomb interaction. In Fig. 14, we plot the energies of the MB states with such simplifications, either based on the U_{ijkl} tensor in the orbital [Fig. 14(a)], or the band [Fig. 14(b)] basis.

Similar to C_BC_N, the case of the orbital basis is better behaved for increasingly simple descriptions of the Coulomb interaction. In this basis, the $|^3A_2\rangle - |^3E\rangle$ triplet-triplet splitting decreases slightly when reducing to a two-coordinate form of the interaction, and then further when an orbitally-averaged interaction is used ["U, U', J" in Fig. 14(a)]. Further simplification of the Coulomb interaction does not change the triplet-triplet splitting. This behavior is likely because the e states are equal superpositions of the dangling bonds on the C atoms around the vacancy [71], so the excited state triplet more or less involves equal population of these states. Interestingly, the first excited state singlet $|^1E\rangle$ energy in Fig. 14(a) is also only mildly effected by the treatment of the interaction, while the energy splitting to the $|^1A_1\rangle$ state is the most sensitive to the treatment of interactions, especially whether or not the interorbital interaction U' is included.

The case of the band basis [Fig. 14(b)] is similar to that of C_BC_N in that Hunds $\mathcal{J}$ is necessary for a description of the entangled $m_s = 0$ triplet states, and the band basis results in a smaller effective on-site $\mathcal{U} = 1.57$ eV, and larger $\mathcal{U}' = 1.10$ eV and $\mathcal{J} = 0.31$ eV than for the orbital basis. Also analogously to C_BC_N, the MR nature of the states are significantly reduced for simplified Coulomb interactions. Most strikingly, we see in Fig. 14(b) that systematic simplification of the interaction, even down to the two-index tensor,

produces an incorrect energetic ordering; this is in contrast to the Wannier-orbital basis [Fig. 14(a)], where the qualitative properties of the MB states are correct even if we use only a single interaction parameter.

C. Summary and implications from test cases

The aim of this paper was to critically analyze the embedding approach for describing the excited states of point defects in the context of the details outlined in Sec. I: (i) the choice of the initial electronic configuration, (ii) procedure for isolating the correlated orbitals, (iii) approach for obtaining the effective Coulomb interaction, and (iv) approach to "double-counting." Below we summarize the implications from our test-case defects in the context of these challenges.

In all cases, numerical convergence was fairly straightforward. The bulk screening in the cRPA could be converged via increasing the number of bands per atom, as well as the k mesh density and/or the supercell size [(iii)]. The MB energies were also relatively insensitive to the details of the Wannierization procedure [(ii)]. Regarding the choice of XC functional, it was clear that the main difference between HSE and PBE for the DFT starting point is the increased splitting in the single particle states in the hybrid functional [(i)]. Even so, using the appropriate DC correction for PBE and HSE resulted in significantly improved agreement between the two starting points [(iv)]. For C_BC_N and NV^-, the resulting MB energies were also in good agreement with available experimental observations. For NV^-, our calculations were consistent with previous embedding implementations [42,43].

Fe_{Al} in AlN constituted the most challenging case, where we showed that the nature of the MB ground and excited states was extremely sensitive to the magnitude of the CFS, which itself was very sensitive to the XC potential of the initial DFT calculation [(i)]. In this case the DC correction was not sufficient to reproduce the expected high-spin ground state with either the PBE or the HSE starting point [(iv)]. We expect that including the PBE XC contribution to the DC will perhaps alleviate this issue. It is also possible that a more accurate treatment of the bulk screening beyond the RPA approximation is necessary, as proposed in Ref. [41] [(iii)]. In any case, Fe_{Al} constitutes a significant challenge to the embedding methodology, and thus an excellent test case for future developments.

VI. CONCLUSIONS

In this paper, we analyzed an embedding approach to treat correlated excited states of point defects. The method is based on Wannierization of density functional theory calculations in order to obtain an active space, including Coulomb interactions in that active space via the constrained RPA method, and correcting for the interaction already included in the DFT part with a functional-dependent double-counting scheme. We showed that this approach provides quantitative accuracy for the C_BC_N defect in BN and NV^- in diamond, although the more complex and sensitive electronic structure of Fe_{Al} in AlN represents a challenge that is out of reach of the present methodology. Overall, despite the complexity and yet unanswered questions about the methodology, we conclude that quantum embedding represents a promising approach to describing the correlated excited states of a variety of point defects in materials.

ACKNOWLEDGMENTS

C.E.D. thanks A. Alkauskas, D. Wickramaratne, M. Zingl, A. Gali, M. Turiansky, T. Berkelbach, and A. Millis for fruitful conversations and comments on the manuscript. The Flatiron Institute is a division of the Simons Foundation. C.E.D. acknowledges support from the National Science Foundation under Grant No. DMR-1918455. The work of D.I.B. was supported by the grant of the President of the Russian Federation, Project No. SP-2488.2021.1.

[1] W. Shockley and W. T. Read, Statistics of the recombinations of holes and electrons, Phys. Rev. **87**, 835 (1952).
[2] R. N. Hall, Electron-hole recombination in Germanium, Phys. Rev. **87**, 387 (1952).
[3] J. R. Weber, W. F. Koehl, J. B. Varley, A. Janotti, B. B. Buckley, C. G. Van de Walle, and D. D. Awschalom, Quantum computing with defects, Proc. Natl. Acad. Sci. USA **107**, 8513 (2010).
[4] B. E. Kane, A silicon-based nuclear spin quantum computer, Nature (London) **393**, 133 (1998).
[5] J. J. Pla, K. Y. Tan, J. P. Dehollain, W. H. Lim, J. J. L. Morton, D. N. Jamieson, A. S. Dzurak, and A. Morello, A single-atom electron spin qubit in silicon, Nature (London) **489**, 541 (2012).
[6] Y. Wu, Y. Wang, X. Qin, X. Rong, and J. Du, A programmable two-qubit solid-state quantum processor under ambient conditions, npj Quantum Inf. **5**, 9 (2019).
[7] I. Aharonovich, S. Castelletto, D. A. Simpson, C.-H. Su, A. D. Greentree, and S. Prawer, Diamond-based single-photon emitters, Rep. Prog. Phys. **74**, 076501 (2011).
[8] I. Aharonovich, A. D. Greentree, and S. Prawer, Diamond photonics, Nat. Photonics **5**, 397 (2011).
[9] R. Schirhagl, K. Chang, M. Loretz, and C. L. Degen, Nitrogen-vacancy centers in diamond: Nanoscale sensors for physics and biology, Annu. Rev. Phys. Chem. **65**, 83 (2014).
[10] M. W. Doherty, N. B. Manson, P. Delaney, F. Jelezko, J. Wrachtrup, and L. C. Hollenberg, The nitrogen-vacancy colour centre in diamond, Phys. Rep. **528**, 1 (2013).
[11] G. Thiering and A. Gali, Theory of the optical spin-polarization loop of the nitrogen-vacancy center in diamond, Phys. Rev. B **98**, 085207 (2018).
[12] A. Alkauskas, C. E. Dreyer, J. L. Lyons, and C. G. Van de Walle, Role of excited states in Shockley-Read-Hall recombination in wide-band-gap semiconductors, Phys. Rev. B **93**, 201304(R) (2016).
[13] D. Wickramaratne, J.-X. Shen, C. E. Dreyer, M. Engel, M. Marsman, G. Kresse, S. Marcinkevičius, A. Alkauskas, and C. G. Van de Walle, Iron as a source of efficient Shockley-

Read-Hall recombination in GaN, Appl. Phys. Lett. **109**, 162107 (2016).
[14] C. E. Dreyer, A. Alkauskas, J. L. Lyons, A. Janotti, and C. G. Van de Walle, First-principles calculations of point defects for quantum technologies, Annu. Rev. Mater. Res. **48**, 1 (2018).
[15] C. Freysoldt, B. Grabowski, T. Hickel, J. Neugebauer, G. Kresse, A. Janotti, and C. G. Van de Walle, First-principles calculations for point defects in solids, Rev. Mod. Phys. **86**, 253 (2014).
[16] W. Kohn and L. J. Sham, Self-consistent equations including exchange and correlation effects, Phys. Rev. **140**, A1133 (1965).
[17] J. P. Perdew and A. Zunger, Self-interaction correction to density-functional approximations for many-electron systems, Phys. Rev. B **23**, 5048 (1981).
[18] P. Mori-Sánchez, A. J. Cohen, and W. Yang, Localization and Delocalization Errors in Density Functional Theory and Implications for Band-Gap Prediction, Phys. Rev. Lett. **100**, 146401 (2008).
[19] U. von Barth, Local-density theory of multiplet structure, Phys. Rev. A **20**, 1693 (1979).
[20] J. Lischner, J. Deslippe, M. Jain, and S. G. Louie, First-Principles Calculations of Quasiparticle Excitations of Open-Shell Condensed Matter Systems, Phys. Rev. Lett. **109**, 036406 (2012).
[21] Q. Sun and G. K.-L. Chan, Quantum embedding theories, Accounts Chem. Res. **49**, 2705 (2016).
[22] L. O. Jones, M. A. Mosquera, G. C. Schatz, and M. A. Ratner, Embedding methods for quantum chemistry: Applications from materials to life sciences, J. Am. Chem. Soc. **142**, 3281 (2020).
[23] J. L. Pascual, L. Seijo, and Z. Barandiarán, *Ab initio* model potential study of the optical absorption spectrum of Mn2+-doped CaF_2, J. Chem. Phys. **103**, 4841 (1995).
[24] R. Llusar, M. Casarrubios, Z. Barandiarán, and L. Seijo, *Ab initio* model potential calculations on the electronic spectrum of Ni2+-doped MgO including correlation, spin–orbit and embedding effects, J. Chem. Phys. **105**, 5321 (1996).
[25] T. Klüner, N. Govind, Y. A. Wang, and E. A. Carter, Periodic density functional embedding theory for complete active space self-consistent field and configuration interaction calculations: Ground and excited states, J. Chem. Phys. **116**, 42 (2002).
[26] D. Muñoz Ramo, J. L. Gavartin, A. L. Shluger, and G. Bersuker, Spectroscopic properties of oxygen vacancies in monoclinic HfO_2 calculated with periodic and embedded cluster density functional theory, Phys. Rev. B **75**, 205336 (2007).
[27] A. S. P. Gomes, C. R. Jacob, and L. Visscher, Calculation of local excitations in large systems by embedding wave-function theory in density-functional theory, Phys. Chem. Chem. Phys. **10**, 5353 (2008).
[28] B. Swerts, L. F. Chibotaru, R. Lindh, L. Seijo, Z. Barandiaran, S. Clima, K. Pierloot, and M. F. A. Hendrickx, Embedding fragment ab initio model potentials in CASSCF/CASPT2 calculations of doped solids: Implementation and applications, J. Chem. Theory Comput. **4**, 586 (2008).
[29] P. Huang and E. A. Carter, Advances in correlated electronic structure methods for solids, surfaces, and nanostructures, Annu. Rev. Phys. Chem. **59**, 261 (2008).
[30] J. L. Pascual, N. Barros, Z. Barandiarán, and L. Seijo, Improved embedding *ab initio* model potentials for embedded cluster calculations, J. Phys. Chem. A **113**, 12454 (2009).
[31] A. S. P. Gomes and C. R. Jacob, Quantum-chemical embedding methods for treating local electronic excitations in complex chemical systems, Annu. Rep. Prog. Chem., Sect. C: Phys. Chem. **108**, 222 (2012).
[32] J. D. Goodpaster, T. A. Barnes, F. R. Manby, and T. F. Miller, 3rd, Accurate and systematically improvable density functional theory embedding for correlated wavefunctions, J. Chem. Phys. **140**, 18A507 (2014).
[33] T. Nguyen Lan, A. A. Kananenka, and D. Zgid, Rigorous *ab initio* quantum embedding for quantum chemistry using Green's function theory: Screened interaction, nonlocal self-energy relaxation, orbital basis, and chemical accuracy, J. Chem. Theory Comput. **12**, 4856 (2016).
[34] M. Dvorak, D. Golze, and P. Rinke, Quantum embedding theory in the screened coulomb interaction: Combining configuration interaction with BSE, Phys. Rev. Materials **3**, 070801(R) (2019).
[35] Z.-H. Cui, T. Zhu, and G. K.-L. Chan, Efficient implementation of *ab initio* quantum embedding in periodic systems: Density matrix embedding theory, J. Chem. Theory Comput. **16**, 119 (2020).
[36] P. V. Sriluckshmy, M. Nusspickel, E. Fertitta, and G. H. Booth, Fully algebraic and self-consistent effective dynamics in a static quantum embedding, Phys. Rev. B **103**, 085131 (2021).
[37] N. He, C. Li, and F. A. Evangelista, Second-order active-space embedding theory, J. Chem. Theory Comput. **18**, 1527 (2022).
[38] G. Kotliar, S. Y. Savrasov, K. Haule, V. S. Oudovenko, O. Parcollet, and C. A. Marianetti, Electronic structure calculations with dynamical mean-field theory, Rev. Mod. Phys. **78**, 865 (2006).
[39] K. Haule, Structural predictions for correlated electron materials using the functional dynamical mean field theory approach, J. Phys. Soc. Jpn. **87**, 041005 (2018).
[40] K. Held, Electronic structure calculations using dynamical mean field theory, Adv. Phys. **56**, 829 (2007).
[41] H. Ma, N. Sheng, M. Govoni, and G. Galli, Quantum embedding theory for strongly correlated states in materials, J. Chem. Theory Comput. **17**, 2116 (2021).
[42] M. Bockstedte, F. Schütz, T. Garratt, V. Ivády, and A. Gali, *Ab initio* description of highly correlated states in defects for realizing quantum bits, npj Quantum Mater. **3**, 31 (2018).
[43] H. Ma, M. Govoni, and G. Galli, Quantum simulations of materials on near-term quantum computers, npj Comput. Mater. **6**, 85 (2020).
[44] H. Ma, N. Sheng, M. Govoni, and G. Galli, First-principles studies of strongly correlated states in defect spin qubits in diamond, Phys. Chem. Chem. Phys. **22**, 25522 (2020).
[45] G. Barcza, V. Ivády, T. Szilvási, M. Voros, L. Veis, Á. Gali, and O. Legeza, DMRG on top of plane-wave Kohn–Sham orbitals: A case study of defected boron nitride, J. Chem. Theory Comput. **17**, 1143 (2021).
[46] W. Pfäffle, D. Antonov, J. Wrachtrup, and G. Bester, Screened configuration interaction method for open-shell excited states applied to NV centers, Phys. Rev. B **104**, 104105 (2021).

[47] S. Gardonio, M. Karolak, T. O. Wehling, L. Petaccia, S. Lizzit, A. Goldoni, A. I. Lichtenstein, and C. Carbone, Excitation Spectra of Transition-Metal Atoms on the Ag (100) Surface Controlled by Hund's Exchange, Phys. Rev. Lett. **110**, 186404 (2013).

[48] F. Ma, W. Purwanto, S. Zhang, and H. Krakauer, Quantum Monte Carlo Calculations in Solids with Downfolded Hamiltonians, Phys. Rev. Lett. **114**, 226401 (2015).

[49] B. Eskridge, H. Krakauer, and S. Zhang, Local embedding and effective downfolding in the auxiliary-field quantum Monte Carlo method, J. Chem. Theory Comput. **15**, 3949 (2019).

[50] Y. Virgus, W. Purwanto, H. Krakauer, and S. Zhang, *Ab initio* many-body study of cobalt adatoms adsorbed on graphene, Phys. Rev. B **86**, 241406(R) (2012).

[51] Y. Virgus, W. Purwanto, H. Krakauer, and S. Zhang, Stability, Energetics, and Magnetic States of Cobalt Adatoms on Graphene, Phys. Rev. Lett. **113**, 175502 (2014).

[52] X. Zhang and E. A. Carter, Subspace density matrix functional embedding theory: Theory, implementation, and applications to molecular systems, J. Chem. Theory Comput. **15**, 949 (2019).

[53] T. Schäfer, F. Libisch, G. Kresse, and A. Grüneis, Local embedding of coupled cluster theory into the random phase approximation using plane waves, J. Chem. Phys. **154**, 011101 (2021).

[54] T. Schäfer, A. Gallo, A. Irmler, F. Hummel, and A. Grüneis, Surface science using coupled cluster theory via local Wannier functions and in-RPA-embedding: The case of water on graphitic carbon nitride, J. Chem. Phys. **155**, 244103 (2021).

[55] B. T. Lau, G. Knizia, and T. C. Berkelbach, Regional embedding enables high-level quantum chemistry for surface science, J. Phys. Chem. Lett. **12**, 1104 (2021).

[56] F. Aryasetiawan, K. Karlsson, O. Jepsen, and U. Schönberger, Calculations of Hubbard u from first-principles, Phys. Rev. B **74**, 125106 (2006).

[57] T. Zhu and Garnet Kin-Lic Chan, *Ab initio* Full Cell gw + DMFT for Correlated Materials, Phys. Rev. X **11**, 021006 (2021).

[58] F. Aryasetiawan, M. Imada, A. Georges, G. Kotliar, S. Biermann, and A. I. Lichtenstein, Frequency-dependent local interactions and low-energy effective models from electronic structure calculations, Phys. Rev. B **70**, 195104 (2004).

[59] M. Karolak, G. Ulm, T. Wehling, V. Mazurenko, A. Poteryaev, and A. Lichtenstein, Double counting in LDA+DMFT-the example of NiO, J. Electron Spectrosc. Relat. Phenom. **181**, 11 (2010).

[60] K. Haule, Exact Double Counting in Combining the Dynamical Mean Field Theory and the Density Functional Theory, Phys. Rev. Lett. **115**, 196403 (2015).

[61] See Supplemental Material http://link.aps.org/supplemental/10.1103/PhysRevB.105.235104 for computational parameters, details of the many-body states, and methodology for calculating symmetry of the many body states, which includes Refs. [117–122].

[62] K. Era, F. Minami, and T. Kuzuba, Fast luminescence from carbon-related defects of hexagonal boron nitride, J. Lumin. **24-25**, 71 (1981).

[63] L. Museur, E. Feldbach, and A. Kanaev, Defect-related photoluminescence of hexagonal boron nitride, Phys. Rev. B **78**, 155204 (2008).

[64] X. Z. Du, J. Li, J. Y. Lin, and H. X. Jiang, The origin of deep-level impurity transitions in hexagonal boron nitride, Appl. Phys. Lett. **106**, 021110 (2015).

[65] M. Mackoit-Sinkevičienė, M. Maciaszek, C. G. Van de Walle, and A. Alkauskas, Carbon dimer defect as a source of the 4.1 eV luminescence in hexagonal boron nitride, Appl. Phys. Lett. **115**, 212101 (2019).

[66] C. Linderälv, W. Wieczorek, and P. Erhart, Vibrational signatures for the identification of single-photon emitters in hexagonal boron nitride, Phys. Rev. B **103**, 115421 (2021).

[67] C. Jara, T. Rauch, S. Botti, M. A. L. Marques, A. Norambuena, R. Coto, J. E. Castellanos-Águila, J. R. Maze, and F. Munoz, First-principles identification of single photon emitters based on carbon clusters in hexagonal boron nitride, J. Phys. Chem. A **125**, 1325 (2021).

[68] Á. Gali, *Ab initio* theory of the nitrogen-vacancy center in diamond, Nanophotonics **8**, 154 (2019).

[69] V. Acosta and P. Hemmer, Nitrogen-vacancy centers: Physics and applications, MRS Bull. **38**, 127 (2013).

[70] M. W. Doherty, N. B. Manson, P. Delaney, and L. C. L. Hollenberg, The negatively charged nitrogen-vacancy centre in diamond: The electronic solution, New J. Phys. **13**, 025019 (2011).

[71] J. R. Maze, A. Gali, E. Togan, Y. Chu, A. Trifonov, E. Kaxiras, and M. D. Lukin, Properties of nitrogen-vacancy centers in diamond: The group theoretic approach, New J. Phys. **13**, 025025 (2011).

[72] C. Bhandari, A. L. Wysocki, S. E. Economou, P. Dev, and K. Park, Multiconfigurational study of the negatively charged nitrogen-vacancy center in diamond, Phys. Rev. B **103**, 014115 (2021).

[73] G. Thiering and A. Gali, *Ab initio* calculation of spin-orbit coupling for an NV center in diamond exhibiting dynamic Jahn-Teller effect, Phys. Rev. B **96**, 081115(R) (2017).

[74] E. R. Weber, Transition metals in silicon, Appl. Phys. A **30**, 1 (1983).

[75] T. H. Maiman, Stimulated optical radiation in ruby, Nature (London) **187**, 493 (1960).

[76] D. Wickramaratne, J.-X. Shen, C. E. Dreyer, A. Alkauskas, and C. G. Van de Walle, Electrical and optical properties of iron in GaN, AlN, and InN, Phys. Rev. B **99**, 205202 (2019).

[77] S. Sugano, Y. Tanabe, and H. Kamimura, *Multiplets of Transition-Metal Ions in Crystals* (Academic Press, New York, 1970).

[78] E. Malguth, A. Hoffmann, W. Gehlhoff, O. Gelhausen, M. R. Phillips, and X. Xu, Structural and electronic properties of Fe3+ and Fe2+ centers in GaN from optical and EPR experiments, Phys. Rev. B **74**, 165202 (2006).

[79] E. Malguth, A. Hoffmann, and M. R. Phillips, Fe in III-V and II-VI semiconductors, phys. stat. sol. (b) **245**, 455 (2008).

[80] B. Neuschl, M. L. Gödecke, K. Thonke, F. Lipski, M. Klein, F. Scholz, and M. Feneberg, Zeeman spectroscopy of the internal transition $^4T_1$ to $^6A_1$ of Fe3+ ions in wurtzite GaN, J. Appl. Phys. **118**, 215705 (2015).

[81] T. Zakrzewski and P. Boguslawski, Electronic structure of transition metal ions in GaN and AlN: Comparing GGA+U with experiment, J. Alloys Compd. **664**, 565 (2016).

[82] J. Baur, K. Maier, M. Kunzer, U. Kaufmann, and J. Schneider, Determination of the GaN/AlN band offset via the $(-/0)$ acceptor level of iron, Appl. Phys. Lett. **65**, 2211 (1994).

[83] V. A. Soltamov, I. V. Ilyin, A. A. Soltamova, E. N. Mokhov, and P. G. Baranov, Identification of the deep level defects in AlN single crystals by electron paramagnetic resonance, J. Appl. Phys. **107**, 113515 (2010).

[84] H. Masenda, D. Naidoo, K. Bharuth-Ram, H. Gunnlaugsson, K. Johnston, R. Mantovan, T. Mølholt, M. Ncube, S. Shayestehaminzadeh, H. Gíslason *et al.*, Lattice sites, charge states and spin-lattice relaxation of Fe ions in $^{57}Mn^{+}$ implanted GaN and AlN, J. Magn. Magn. Mater. **401**, 1130 (2016).

[85] R. P. Messmer and G. D. Watkins, Linear Combination of Atomic Orbital-Molecular Orbital Treatment of the Deep Defect Level in a Semiconductor: Nitrogen in Diamond, Phys. Rev. Lett. **25**, 656 (1970).

[86] S. G. Louie, M. Schlüter, J. R. Chelikowsky, and M. L. Cohen, Self-consistent electronic states for reconstructed Si vacancy models, Phys. Rev. B **13**, 1654 (1976).

[87] G. Kresse and J. Hafner, *Ab initio* molecular dynamics for liquid metals, Phys. Rev. B **47**, 558 (1993).

[88] G. Kresse and J. Furthmüller, Efficient iterative schemes for *ab initio* total-energy calculations using a plane-wave basis set, Phys. Rev. B **54**, 11169 (1996).

[89] G. Kresse and D. Joubert, From ultrasoft pseudopotentials to the projector augmented-wave method, Phys. Rev. B **59**, 1758 (1999).

[90] A. A. Mostofi, J. R. Yates, G. Pizzi, Y.-S. Lee, I. Souza, D. Vanderbilt, and N. Marzari, An updated version of WANNIER90: A tool for obtaining maximally-localised Wannier functions, Comput. Phys. Commun. **185**, 2309 (2014).

[91] M. Kaltak, Merging GW with DMFT, Ph.D. thesis, University of Vienna, 2015.

[92] O. Parcollet, M. Ferrero, T. Ayral, H. Hafermann, I. Krivenko, L. Messio, and P. Seth, TRIQS: a toolbox for research on interacting quantum systems, Comput. Phys. Commun. **196**, 398 (2015).

[93] M. I. Katsnelson and A. I. Lichtenstein, LDA + + approach to the electronic structure of magnets: correlation effects in iron, J. Phys.: Condens. Matter **11**, 1037 (1999).

[94] J. Heyd, G. E. Scuseria, and M. Ernzerhof, Hybrid functionals based on a screened coulomb potential, J. Chem. Phys. **118**, 8207 (2003).

[95] J. Heyd, G. E. Scuseria, and M. Ernzerhof, Erratum: Hybrid functionals based on a screened Coulomb potential [J. Chem. Phys. 118, 8207 (2003)], J. Chem. Phys. **124**, 219906 (2006).

[96] A. J. Garza and G. E. Scuseria, Predicting band gaps with hybrid density functionals, J. Phys. Chem. Lett. **7**, 4165 (2016).

[97] J. P. Perdew, K. Burke, and M. Ernzerhof, Generalized Gradient Approximation Made Simple, Phys. Rev. Lett. **77**, 3865 (1996).

[98] A. M. Stoneham, *Theory of Defects in Solids: Electronic Structure of Defects in Insulators and Semiconductors* (Oxford University Press, Oxford, 2001).

[99] G. Davies, Optical measurements of point defects, in *Identification of Defects in Semiconductors*, edited by M. Stravola (Academic Press, New York, 1999), Chap. 1.

[100] A. Alkauskas, M. D. McCluskey, and C. G. Van de Walle, Tutorial: Defects in semiconductors–combining experiment and theory, J. Appl. Phys. **119**, 181101 (2016).

[101] A. Alkauskas, B. B. Buckley, D. D. Awschalom, and C. G. Van de Walle, First-principles theory of the luminescence lineshape for the triplet transition in diamond NV centres, New J. Phys. **16**, 073026 (2014).

[102] E. Şaşıoğlu, C. Friedrich, and S. Blügel, Effective Coulomb interaction in transition metals from constrained random-phase approximation, Phys. Rev. B **83**, 121101(R) (2011).

[103] E. G. C. P. van Loon, M. Rösner, M. I. Katsnelson, and T. O. Wehling, Random phase approximation for gapped systems: Role of vertex corrections and applicability of the constrained random phase approximation, Phys. Rev. B **104**, 045134 (2021).

[104] F. Hüser, T. Olsen, and K. S. Thygesen, How dielectric screening in two-dimensional crystals affects the convergence of excited-state calculations: Monolayer MoS_2, Phys. Rev. B **88**, 245309 (2013).

[105] K. Andersen, S. Latini, and K. S. Thygesen, Dielectric genome of van der Waals heterostructures, Nano Lett. **15**, 4616 (2015).

[106] M. Rösner, E. Şaşıoğlu, C. Friedrich, S. Blügel, and T. O. Wehling, Wannier function approach to realistic coulomb interactions in layered materials and heterostructures, Phys. Rev. B **92**, 085102 (2015).

[107] This hopping is out of plane, and can be reduced to 3 meV by doubling the cell in the c direction. However, we find that using a larger cell in $\hat{c}$ does not significantly change the MB energies (<20 meV).

[108] J. H. Skone, M. Govoni, and G. Galli, Self-consistent hybrid functional for condensed systems, Phys. Rev. B **89**, 195112 (2014).

[109] A. Gali, E. Janzén, P. Deák, G. Kresse, and E. Kaxiras, Theory of Spin-Conserving Excitation of the NV Center in Diamond, Phys. Rev. Lett. **103**, 186404 (2009).

[110] A. I. Liechtenstein, V. I. Anisimov, and J. Zaanen, Density-functional theory and strong interactions: Orbital ordering in Mott-Hubbard insulators, Phys. Rev. B **52**, R5467 (1995).

[111] I. A. Nekrasov, V. Pavlov, and M. V. Sadovskii, Consistent LDA+DMFT–an unambiguous way to avoid double counting problem: NiO test, JETP Lett. **95**, 581 (2012).

[112] O. Kristanovski, A. B. Shick, F. Lechermann, and A. I. Lichtenstein, Role of nonspherical double counting in DFT+DMFT: Total energy and structural optimization of pnictide superconductors, Phys. Rev. B **97**, 201116(R) (2018).

[113] A. Szabó and N. Ostlund, *Modern Quantum Chemistry: Introduction to Advanced Electronic Structure Theory* (Dover Publications, Mineola, NY, 1996).

[114] Y. Ma and M. Rohlfing, Optical excitation of deep defect levels in insulators within many-body perturbation theory: The F center in calcium fluoride, Phys. Rev. B **77**, 115118 (2008).

[115] D. J. Carrascal, J. Ferrer, J. C. Smith, and K. Burke, The Hubbard dimer: A density functional case study of a many-body problem, J. Phys.: Condens. Matter **27**, 393001 (2015).

[116] L. E. Ballentine, *Quantum Mechanics: A Modern Development* (World Scientific Publishing Company, Singapore, 2014).

[117] C. E. Dreyer, J. L. Lyons, A. Janotti, and C. G. Van de Walle, Band alignments and polarization properties of BN polymorphs, Appl. Phys. Express **7**, 031001 (2014).

[118] L. Razinkovas, M. W. Doherty, N. B. Manson, C. G. Van de Walle, and A. Alkauskas, Vibrational and

vibronic structure of isolated point defects: The nitrogen-vacancy center in diamond, Phys. Rev. B **104**, 045303 (2021).

[119] C. Freysoldt, J. Neugebauer, and C. G. Van de Walle, Fully *Ab Initio* Finite-Size Corrections for Charged-Defect Supercell Calculations, Phys. Rev. Lett. **102**, 016402 (2009).

[120] M. Schüler, M. Rösner, T. O. Wehling, A. I. Lichtenstein, and M. I. Katsnelson, Optimal Hubbard Models for Materials with Nonlocal Coulomb Interactions: Graphene, Silicene, and Benzene, Phys. Rev. Lett. **111**, 036601 (2013).

[121] J. P. Goss, R. Jones, S. J. Breuer, P. R. Briddon, and S. Öberg, The Twelve-Line 1.682 eV Luminescence Center in Diamond and the Vacancy-Silicon Complex, Phys. Rev. Lett. **77**, 3041 (1996).

[122] M. Maciaszek, L. Razinkovas, and A. Alkauskas, Thermodynamics of carbon point defects in hexagonal boron nitride, Phys. Rev. Materials **6**, 014005 (2022).